Early science with the Large Millimeter Telescope: a 1.1 mm AzTEC survey of red-*Herschel* dusty star-forming galaxies

A. Montaña [1,2]★ J. A. Zavala [3] I. Aretxaga,[2] D. H. Hughes,[2] R. J. Ivison [4] A. Pope,[5]
D. Sánchez-Argüelles,[1,2] G. W. Wilson,[5] M. Yun [5] O. A. Cantua,[3] M. McCrackan,[5] M. J. Michałowski,[6]
E. Valiante,[7] V. Arumugam,[8] C. M. Casey,[3] R. Chávez,[1,9] E. Colín-Beltrán,[1,2] H. Dannerbauer,[10,11]
J. S. Dunlop,[12] L. Dunne,[13] S. Eales,[13] D. Ferrusca,[2] V. Gómez-Rivera,[2]
A. I. Gómez-Ruiz,[1,2] V. H. de la Luz,[14] S. J. Maddox,[12,13] G. Narayanan,[5] A. Omont,[15]
I. Rodríguez-Montoya,[1,2] S. Serjeant [16] F. P. Schloerb,[5] M. Velázquez,[2] S. Ventura-González,[17]
P. van der Werf[18] and M. Zeballos [2,19]

Affiliations are listed at the end of the paper

ABSTRACT

We present Large Millimeter Telescope (*LMT*)/AzTEC 1.1 mm observations of ∼100 luminous high-redshift dusty star-forming galaxy candidates from the ∼ 600 sq.deg *Herschel*-ATLAS survey, selected on the basis of their SPIRE red far-infrared colours and with $S_{500\,\mu m} = 35 - 80$ mJy. With an effective $\theta_{FWHM} \approx 9.5$ arcsec angular resolution, our observations reveal that at least 9 per cent of the targets break into multiple systems with signal-to-noise ratio ≥4 members. The fraction of multiple systems increases to ∼23 per cent (or more) if some non-detected targets are considered multiples, as suggested by the data. Combining the new AzTEC and deblended *Herschel* photometry, we derive photometric redshifts, infrared luminosities, and star formation rates. While the median redshifts of the multiple and single systems are similar ($z_{med} \approx 3.6$), the redshift distribution of the latter is skewed towards higher redshifts. Of the AzTEC sources, ∼85 per cent lie at $z_{phot} > 3$ while ∼33 per cent are at $z_{phot} > 4$. This corresponds to a lower limit on the space density of ultrared sources at $4 < z < 6$ of ∼ 3×10^{-7} Mpc^{-3} with a contribution to the obscured star formation of $\gtrsim 8 \times 10^{-4}$ M$_\odot$ yr^{-1} Mpc^{-3}. Some of the multiple systems have members with photometric redshifts consistent among them suggesting possible physical associations. Given their angular separations, these systems are most likely galaxy over-densities and/or early-stage pre-coalescence mergers. Finally, we present 3 mm LMT/RSR spectroscopic redshifts of six red-*Herschel* galaxies at $z_{spec} = 3.85-6.03$, two of them (at $z \sim 4.7$) representing new redshift confirmations. Here, we release the AzTEC and deblended *Herschel* photometry as well as catalogues of the most promising interacting systems and $z > 4$ galaxies.

Key words: galaxies: high-redshift – galaxies: interactions – galaxies: starburst – submillimetre: galaxies.

1 INTRODUCTION

Taking advantage of a narrow atmospheric window at $\lambda \approx 850\,\mu m$, around two decades ago, the first surveys taken at submillimetre wavelengths with the SCUBA camera – which now sits in the National Museum of Scotland in Edinburgh – confirmed the existence of a population of high-redshift dust-enshrouded star-forming galaxies (e.g. Smail, Ivison & Blain 1997; Barger et al. 1998; Hughes et al. 1998).

Thanks to the significant two-decade effort poured into determining the physical properties of these galaxies, it is now known that they show the most extreme star formation rates (SFR; from 100's to 1000's M$_\odot$ yr^{-1}) in the Universe (modulo the possibility of a very top heavy stellar initial mass function (IMF), e.g. Zhang et al. 2018), have large stellar and dust masses (∼10^{10-11} and ∼10^{8-9}

M$_\odot$, respectively) with large gas mass reservoirs (∼10^{10-11} M$_\odot$), and contribute significantly to the cosmic SFR density (see reviews by Casey, Narayanan & Cooray 2014 and Hodge & da Cunha 2020). These sources are also considered to be the progenitors of massive, quiescent galaxies observed at $z \approx 2-3$, which ultimately lead to the assembly of the massive elliptical galaxies observed in the local Universe (Toft et al. 2014; Simpson et al. 2014).

Nevertheless, despite their recognized importance in our understanding of galaxy formation and evolution, fundamental questions remain unanswered. For example, although the bulk of the population is known to lie at $z \approx 2-4$ (e.g. Aretxaga et al. 2003; Chapman et al. 2005; Aretxaga et al. 2007; Michałowski et al. 2012; Yun et al. 2012; Simpson et al. 2014; Koprowski et al. 2016; Brisbin et al. 2017; Zavala et al. 2018b; Dudzevičiūtė et al. 2020; Simpson et al. 2020), their distribution at high redshifts ($z > 4$) and its dependence with flux density remains unclear. Constraining the prevalence of these galaxies is crucial, for in-

★ E-mail: amontana@inaoep.mx

stance, to derive a complete census of the cosmic SFR density and to test our current models of cosmic structure formation, since these galaxies are expected to trace the assembly of the first massive dark matter haloes in the Universe (Marrone et al. 2018).

An important step towards understanding the formation processes that built up these extreme galaxies relies on determining their triggering mechanisms and their star formation modes. Pioneering observational and theoretical studies concluded that the formation scenario of submillimetre galaxies (SMGs) involves major and minor gas-rich mergers (e.g. Tacconi et al. 2006; Ivison et al. 2007; Bothwell et al. 2010; Engel et al. 2010; Narayanan et al. 2010). Nevertheless, subsequent theoretical work showed that early-stage mergers (pre-coalescence galaxy pairs), isolated star-forming discs, and even line-of-sight projections or gravitational lensing can lead to these bright submm fluxes (e.g. Davé et al. 2010; Hayward et al. 2011; Narayanan et al. 2015). Although it is now clear that the population of dusty star-forming galaxies (DSFGs) may be rather heterogeneous (e.g. Hayward et al. 2018; Jiménez-Andrade et al. 2020), the relative importance of each component remains uncertain.

Characterizing these specifics requires sensitive and wide enough surveys to capture the rarest systems, which allow us to test the predictions from galaxy-formation models (e.g. Hayward 2013; Gruppioni et al. 2015; Lacey et al. 2016; Lagos et al. 2019; McAlpine et al. 2019).

The large-area surveys conducted with the *Herschel* Space Observatory (as well as the South Pole Telescope – *SPT*; Vieira et al. 2010) have already identified remarkable examples of such systems, including some of the most distant dusty galaxies currently known at $z \approx 6-7$ (Riechers et al. 2013; Fudamoto et al. 2017; Zavala et al. 2018a) and extreme galaxy over-densities (i.e. proto-cluster structures) in the early Universe (e.g. Ivison et al. 2013; Oteo et al. 2018; see Strandet et al. 2017 and Miller et al. 2018 for similar systems selected by the *SPT*). Part of this success relies on the availability of simultaneous observations at 250, 350, and 500 µm with the Spectral and Photometric Imaging Receiver (SPIRE), which enable a straightforward selection criteria ($S_{250\,\mu m} < S_{350\,\mu m} < S_{500\,\mu m}$) of high-redshift candidates known as '500 µm risers' or 'red-*Herschel* galaxies' (e.g. Pope & Chary 2010; Cox et al. 2011; Dowell et al. 2014; Asboth et al. 2016; Ivison et al. 2016; Donevski et al. 2018; Duivenvoorden et al. 2018; Ma et al. 2019; Bakx et al. 2020b).

Follow-up observations with higher angular resolutions at (ideally) longer wavelengths than those used to select these galaxies are, however, necessary as an intermediate step to identify and filter out possible contaminants, whilst providing more accurate positions for spectroscopic surveys. Previous works, as those discussed in more detail below, have focused on samples of red-*Herschel* sources followed-up with the SCUBA-2 camera at 850 µm ($\theta_{FWHM} \approx$ 15 arcsec), LABOCA at 870 µm ($\theta_{FWHM} \approx$ 19 arcsec; Dowell et al. 2014; Asboth et al. 2016; Ivison et al. 2016; Donevski et al. 2018; Duivenvoorden et al. 2018), or with higher angular resolution interferometric observations with ALMA, NOEMA and the SMA (e.g. Ma et al. 2019; Greenslade et al. 2020).

Here, we present 1.1 mm imaging, using the Aztronomical Thermal Emission Camera (AzTEC, Wilson et al. 2008) on the Large Millimeter Telescope (LMT;[1] Hughes et al. 2010) of a relatively large sample of 100 *Herschel*-selected galaxies. Additionally, we present 3 mm spectra of six red-*Herschel* sources using the Redshift Search Receiver (RSR). We provide new redshifts for two of these

[1] www.lmtgtm.org

sources (with $z \gtrsim 4.7$) and confirm the redshift of the other 4, which were already known (Fudamoto et al. 2017; Zavala et al. 2018a).

The 32-m illuminated surface of the telescope, at the time of the observations, provides an effective angular resolution of $\theta_{FWHM} \approx 9.5$ arcsec, a factor of 4 better than *Herschel* at 500 µm ($\theta_{FWHM} \approx 36$ arcsec). This angular resolution enables the identification of not only the most promising high-redshift candidates but also of physically interacting galaxies blended within the *Herschel* beam, as discussed below.

This paper is structured as follows: Section 2 describes the sample selection and AzTEC/RSR observations. The analysis of these images and the bulk of the results are presented in Section 3. This includes constraints on the multiplicity, as well as photometric redshift, luminosity, and SFR estimations. In Section 4, we identify and present sub-samples of the most promising high-redshift candidates and physically interacting galaxies. Finally, the implications of these results in our general understanding of the properties of this population of galaxies are discussed in Section 5, where our conclusions are also summarized.

Throughout this paper, we assume a flat ΛCDM cosmology with $H_0 = 68\,km\,s^{-1}\,Mpc^{-1}$ and $\Omega_\Lambda = 0.69$ (Planck Collaboration 2016), and the Chabrier (2003) IMF for SFR estimations.

## 2 SAMPLE AND OBSERVATIONS

2.1 Sample selection

The *Herschel* Astrophysical Terahertz Large Area Survey (*H*-ATLAS; Eales et al. 2010; Valiante et al. 2016) is one of the largest surveys ($\sim 600\,deg^2$) carried out with the *Herschel* Space Observatory. The thousands of sources detected at 250, 350, and 500 µm in the South Galactic Pole (SGP), North Galactic Pole (NGP), and the Galaxy and Mass Assembly 9 h (G09), 12 h (G12), and 15 h (G15) fields, make *H*-ATLAS an ideal survey to search for rare high redshift ($z \gtrsim 4$) DSFGs.

Our sample was taken from a parent sample of ultrared DSFGs obtained by Ivison et al. (2016), where a detailed description of the selection process is presented and summarized here. First, candidates at $>2.2\sigma$ were identified in the 250 µm maps using the Multiband Algorithm for source eXtraction (Maddox & Dunne 2020). Then, PSFs with scaled flux densities at each band were subtracted from the SPIRE maps. Subsequently, a second and third set of candidates were generated by repeating the process and searching for $>2.4\sigma$ and $>3.5\sigma$ peaks in the 350 and 500 µm residual maps, respectively. The final catalogue of 7961 ultrared sources includes only those detected at $\geq 3.5\sigma$ at 500 µm and with $S_{500\,\mu m}/S_{250\,\mu m} \geq 1.5$ and $S_{500\,\mu m}/S_{350\,\mu m} \geq 0.85$. A sub-sample of 2725 ultrared candidates was eyeballed to find a reliable sample for ground-based observations. It is important to note that the eyeballing process rejected 22 per cent of the candidates which were heavily confused and whose flux densities (and therefore colours) were unreliable (see Ivison et al. 2016 for details).

This colour selected sources with spectral energy distributions (SEDs) that rise from 250 to 350 µm and continue rising onwards to 500 µm ($S_{250\,\mu m} < S_{350\,\mu m} < S_{500\,\mu m}$) are called '500 µm risers' or red-*Herschel* sources. This technique enabled the identification of DSFGs up to $z \sim 6$ (e.g. Riechers et al. 2013; Asboth et al. 2016; Zavala et al. 2018a).

The final sample of 108 ultrared *Herschel* sources selected for LMT follow-up observations has signal-to-noise ratios (SNR) at 500 µm $\gtrsim 5$ and colour cuts $S_{500\,\mu m}/S_{250\,\mu m} > 2$ and $S_{500\,\mu m}/S_{350\,\mu m} > 1$ (see Fig. 1). Most of the sample (~ 80 per cent)
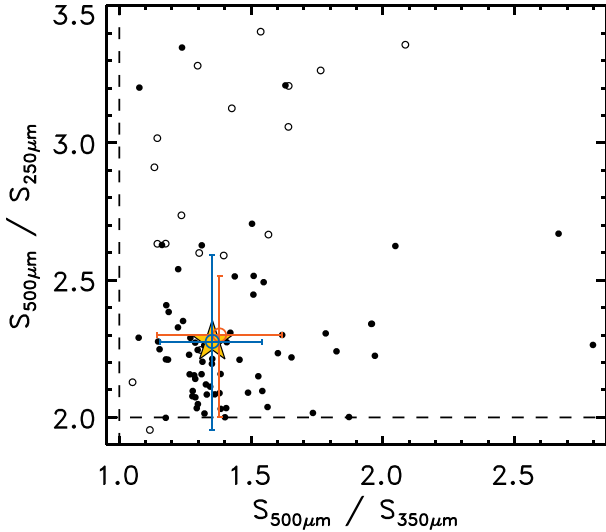
Figure 1. Colour selection ($S_{500\,\mu m}/S_{250\,\mu m} > 2$ and $S_{500\,\mu m}/S_{350\,\mu m} > 1$) of the *H*-ATLAS targets observed with AzTEC: filled black circles identified in the 250 μm map and empty circles in the 350 μm (i.e. BANDFLAG 1 and 2 in Ivison et al. (2016), respectively). All targets were detected above 5σ at 500 μm. The yellow star indicates the average colour of the sample, while the blue and orange circles indicate, respectively, the median colour of the targets with and without AzTEC detections above a 4σ level. The similar colours shown by the two sub-samples suggest that differences in SEDs cannot explain the bulk of AzTEC non-detections discussed in Section 3.2.

were identified in the 250 μm map, with the remaining ones identified in the 350 μm residual maps (Fig. 1). An additional selection criteria of 35 mJy < $S_{500\,\mu m}$ < 80 mJy was imposed to minimize the contamination by false detections and by gravitationally lensed sources, since the fraction of lensed galaxies falls with decreasing 500 μm flux density (with ∼100 per cent of lensed galaxies expected at $S_{500\,\mu m} > 100$ mJy, and ∼50 per cent at $S_{500\,\mu m} > 55$ mJy; Negrello et al. 2010; see also Wardlow et al. 2013; Negrello et al. 2017; Bakx, Eales & Amvrosiadis 2020a). The sample was also checked not to have contamination by radio-loud active galactic nuclei (AGN) and it was correlated with optical/near-infrared (IR) imaging (Bourne et al. 2016) to reject nearby galaxies and any obvious lenses that could have entered the sample. While the contamination by radio-loud AGN is expected to be negligible, gravitationally lensed systems can still be found in the sample (e.g. Donevski et al. 2018). This is because the selection of high-redshift candidates increases the probability of line-of-sight alignment with lower redshift massive structures. Indeed, such lensed systems have been confirmed in the sample (e.g. Zavala et al. 2018a).

2.2 AzTEC observations

Of the 108 targets proposed for the LMT 2014-ES3 campaign (Project 2014AHUGD011, PI: D.H. Hughes), we obtained AzTEC data for 100 sources. AzTEC observations, using the photometry map mode which covers a ∼3.5 arcmin diameter area, were conducted between November 2014 and June 2015 under optimal atmospheric conditions with $\langle \tau_{225\,GHz} \rangle \approx 0.06 \pm 0.02$ ($0.03 \leq \tau_{225\,GHz} \leq 0.11$). The integration times devoted to each target were in the range of 3–50 min (21.3 h in total), with a median of 11 min (Table 1). Pointing measurements on known quasars close to the targets were made before and after science observations, and were used in the data

reduction process to compensate for any pointing drifts, resulting in a rms pointing accuracy ≲ 1 arcsec.

The data were reduced using MACANA, the C++ version of the standard AzTEC data reduction pipeline (e.g. Scott et al. 2008), with a Wiener-filter applied to improve the detection of point-like sources, at the expense of increasing the nominal full width at half-maximum (FWHM) by ∼11 per cent (from ≈8.6 to ≈9.5 arcsec). The AzTEC pipeline produces four main outputs: signal and signal-to-noise maps, a weight map representative of the noise in each pixel of the map, and a 2D transfer function which tracks the effects of the reduction process on the shape of a synthetic 1 Jy point source (i.e. the point spread function [PSF]). Additionally, the pipeline can generate a set of simulated 'jackknifed' noise maps by randomly multiplying the clean time-stream data by ±1. In Section 3.1, we take advantage of these simulations to measure false-detection-rate (FDR) probabilities in our AzTEC maps.

Seven of the targets in the SGP field, observed in the poorest weather conditions ($\tau_{225\,GHz} \approx 0.11$), did not reach the target sensitivity (with $\sigma_{1.1\,mm} > 3.0$ mJy rms) and therefore were removed from the analysis. Thus, we focus on the remaining 93 sources observed with AzTEC (Table 1).

The maps of the final sample have an average depth of $\langle \sigma_{1.1\,mm} \rangle = 1.5 \pm 0.5$ mJy in the central region used for the counterpart analysis (i.e. within the ∼85 per cent coverage area) and $\langle \sigma_{1.1\,mm} \rangle = 2.1 \pm 0.7$ mJy over the 50 per cent coverage area used to detect sources (see Section 3.1). The filtered maps have PSFs with $\langle \theta_{FWHM} \rangle = 9.6 \pm 0.5$ arcsec. Figs 2 and 3 show the 500 μm-flux density distribution of our sample and the attained $\sigma_{1.1\,mm} \approx 0.7 - 2.8$ mJy rms distribution of the AzTEC observations, respectively.

2.3 RSR observations

Six red-*Herschel* sources, confirmed with AzTEC to be single systems at high-redshift ($z_{phot} \gtrsim 4$), were selected for spectroscopic follow-up observations with the RSR on the LMT (Table 2). The RSR is a broadband spectrometer covering the 3 mm window (73–111 GHz) with four detectors in a dual-beam dual-polarization configuration (RSR; Erickson et al. 2007). The observations were done using both the 32 and 50 m (since 2018) configurations of the LMT.

The RSR data were reduced using the Data REduction and Analysis Methods in PYthon package (DREAMPY; written by G. Narayanan) and following the standard procedure (e.g. Yun et al. 2015; Cybulski et al. 2016; Wong et al. 2017). A careful visual inspection of individual scans was performed to identify and remove those with the noisiest spectral features.

We confirm the redshifts presented in Fudamoto et al. (2017) and Zavala et al. (2018a) for four of these sources, and provide two new determinations at $z = 4.768$ and 4.728 (see Table 2). The latter two correspond to G12-26926 and NGP-203484, respectively, whose redshifts are unambiguously identified from at least two emission lines detected with SNR ≥ 5 in each RSR spectrum. Their redshifts are independently confirmed using the template cross-correlation analysis described by Yun et al. (2015). The same template cross-correlation method yields the unique redshifts of three other objects with two or more emission lines in the RSR spectrum (G09-81106, G09-83808, NGP-284347). Only one emission line is detected in the RSR spectrum of NGP-246114, but it is the same CO(4 − 3) line at $z = 3.847$ previously reported by Fudamoto et al. (2017) who also detected a CO(6 − 5) transition. Fig. 4 shows the identified lines in the RSR spectra. Their fitted parameters are summarized in Table 2.

Table 1. Sample of the 93 *H*-ATLAS fields targeted at 1.1 mm with AzTEC (Fig. A1). RA and Dec. (J2000) correspond to the *H*-ATLAS source centroids where the AzTEC maps were centred. The quoted σ_{rms} values correspond to the 85 per cent coverage area of the AzTEC maps (i.e. the ∼36.6 arcsec diameter central area used for our multiplicity analysis).

ID	RA (deg)	Dec. (deg)	t_{int} (min)	σ_{rms} (mJy)	ID	RA (deg)	Dec. (deg)	t_{int} (min)	σ_{rms} (mJy)
G09-12469	140.422 082	0.895 139	30	1.15	NGP-203484[a]	204.917 078	31.369 083	22	1.49
G09-44907	129.345 002	1.429 361	20	0.98	NGP-211862	193.669 996	26.823 668	11	1.62
G09-58643	127.822 924	1.282 944	15	1.20	NGP-222757	199.172 916	23.675 194	11	1.35
G09-62610	137.354 579	1.928 361	30	0.72	NGP-235542	195.640 411	26.673 582	11	1.78
G09-64894	138.189 998	1.195 028	30	1.27	NGP-240219	192.798 743	30.998 196	3	2.67
G09-71054	137.194 161	1.891 806	11	0.89	NGP-244082	199.487 500	34.490 723	11	1.73
G09-75817	130.181 251	1.948 556	11	1.38	NGP-246114[a]	205.309 166	33.992 964	10	1.64
G09-80523	132.810 001	1.034 833	15	1.16	NGP-248192	193.215 837	34.549 946	11	1.55
G09-81106[a]	132.404 541	0.248 816	45	0.82	NGP-248712	197.039 995	22.836 945	11	1.37
G09-83808[a]	135.189 171	0.690 306	11	0.89	NGP-248948	192.160 006	29.628 666	3	2.78
G12-23831	179.638 753	− 1.823 000	15	1.40	NGP-249138	193.611 245	24.625 444	3	2.06
G12-26926[a]	183.489 161	− 1.372 833	11	1.68	NGP-249475	206.234 994	31.441 082	22	1.55
G12-31529	181.649 580	1.549 667	60	1.00	NGP-284357[a]	203.214 926	33.394 179	10	1.54
G12-42911	175.811 248	0.479 556	10	1.60	NGP-49609	203.213 339	32.936 916	3	2.48
G12-47416	182.763 333	0.215 972	22	1.12	NGP-55628	206.604 581	34.270 832	22	1.54
G12-49632	179.715 414	− 0.164 528	22	1.17	NGP-78659	207.216 253	26.899 221	6	2.26
G12-53832	184.296 255	− 0.128 139	3	2.79	NGP-87226	205.289 998	32.933 891	6	2.59
G12-58719	185.308 757	0.930 917	11	1.41	NGP-94843	204.695 005	25.669 167	22	1.44
G12-73303	183.509 173	− 1.932 833	11	1.26	SGP-101187	16.970 000	− 30.297 194	11	1.13
G12-77419	182.271 252	− 1.089 417	6	1.67	SGP-106123	13.851 250	− 28.010 111	26	0.99
G12-78868	179.059 167	1.651 611	3	2.61	SGP-211713	22.584 168	− 31.662 361	15	1.98
G15-23358	214.860 005	0.193 861	11	1.11	SGP-215925	351.983 328	− 32.768 387	11	2.38
G15-26675	221.138 749	0.277 694	6	1.86	SGP-238944	0.077 917	− 33.636 837	11	2.86
G15-29728	211.117 501	1.582 861	11	1.10	SGP-267200	350.531 673	− 34.577 248	11	1.73
G15-48916	214.615 831	0.789 056	11	1.12	SGP-272197	1.531 667	− 32.444 195	15	1.62
G15-57401	214.029 579	1.159 361	11	1.18	SGP-280787	350.393 744	− 33.081 249	11	1.99
G15-63483	221.295 834	0.017 833	11	1.43	SGP-284969	15.858 334	− 30.059 082	26	0.91
G15-68998	222.726 660	− 0.595 778	11	1.27	SGP-289463	25.536 667	− 32.574 276	15	2.07
G15-72333	217.463 751	1.003 722	11	1.07	SGP-293180	18.160 833	− 30.783 361	11	1.22
G15-78944	221.771 665	1.024 111	11	1.28	SGP-316248	354.393 339	− 34.839 191	11	1.43
G15-82597	220.157 919	0.801 556	11	1.31	SGP-322449	344.887 505	− 34.446 335	11	1.34
G15-82610	220.729 165	1.162 305	11	1.45	SGP-323041	18.501 250	− 32.517 056	5	2.16
G15-82660	215.634 999	0.505 694	11	1.08	SGP-340137	344.271 240	− 33.839 111	11	1.24
G15-83272	213.802 500	− 0.276 806	3	1.70	SGP-348040	350.404 987	− 35.024 223	11	1.39
NGP-112775	204.170 423	26.266 306	22	1.38	SGP-352624	19.664 167	− 27.638 889	15	1.47
NGP-113203	196.662 912	28.464 140	22	1.43	SGP-359921	16.919 584	− 28.448 500	11	1.21
NGP-115876	204.650 416	27.546 473	22	1.50	SGP-379994	11.356 249	− 32.554 695	15	1.17
NGP-124539	195.212 088	32.776 001	11	1.67	SGP-384367	21.078 333	− 32.980 335	15	1.13
NGP-131281	193.201 246	34.404 278	18	1.36	SGP-396540	10.270 833	− 28.222 473	11	1.37
NGP-139851	196.441 255	25.498 222	3	2.60	SGP-396663	12.548 333	− 32.482 918	11	1.52
NGP-145039	194.372 921	29.280 277	22	1.32	SGP-396921	16.555 417	− 28.231 222	26	0.95
NGP-149267	203.001 666	26.422 222	22	1.36	SGP-396966	8.878 333	− 31.504 917	15	1.27
NGP-157992	193.517 504	27.177 750	3	2.60	SGP-399383	20.202 917	− 30.976 528	15	1.32
NGP-168019	205.405 412	32.476 780	22	1.59	SGP-400082	8.386 249	− 30.080 584	6	1.39
NGP-172727	196.315 827	25.516 083	3	2.50	SGP-403579	355.064 993	− 30.445 110	6	1.28
NGP-176261	199.242 082	33.915 947	9	1.70	SGP-68123	341.992 092	− 29.945 444	11	1.24
NGP-194548	203.407 087	24.261 639	11	1.32					

[a] Selected for spectroscopic follow-up with the 3 mm RSR (see Table 2).

We use these spectroscopic redshifts in Fig. 10 to characterize the accuracy of our photometric-redshift determinations.

An alternative reduction was produced using a new PYTHON wrapper script developed by D. O. Sánchez-Argüelles for the DREAMPY package, known as RSR_DRIVER.[2] This script aims to provide the LMT user community with a front-end interface to generate RSR scientific-quality data from raw observations. The RSR_DRIVER reduction procedure is very similar to the standard process, and below a brief description is presented.

For each detector the RSR backend records the autocorrelation function (ACF) of the observed sky brightness. It is important to notice that the broad 73–111 GHz bandwidth of the RSR is achieved by dividing it into six bands. The raw data are therefore comprised of six ACFs. The pipeline starts by processing the ACFs using a Fourier transform matrix to reconstruct the spectrum of the astronomical source. At this stage, a user defined low order (≤3) polynomial baseline is computed across each band and subtracted from the

[2]The RSR_DRIVER and its documentation is publicly available at the LMT DEVS github repository https://github.com/LMTdevs/RSR_driver.
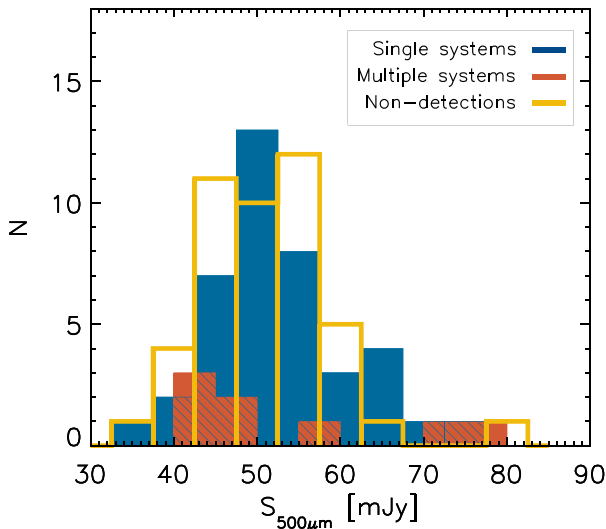
Figure 2. Number of sources as a function of original (before deblending) *Herschel* 500 μm flux density. AzTEC sources classified as single and multiple systems (see Section 3) are illustrated by the blue and orange histograms, while AzTEC non-detections (SNR < 4) are represented by the yellow histogram. As shown, the three different sets include sources with similar flux densities, discarding possible selection biases in the classification. The bins are slightly shifted for better visualization.
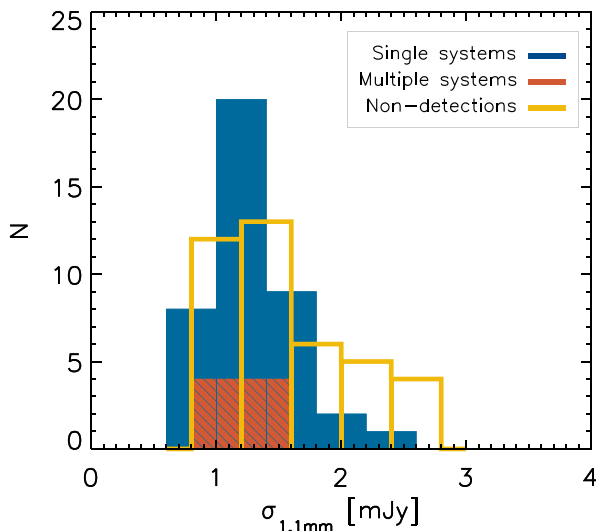
Figure 3. Histogram of achieved sensitivity in the AzTEC observations for the three different classifications: Single systems (in blue), multiple systems (orange), and non-detections (yellow, SNR < 4). Our survey shows an homogeneous sensitivity, with all of the maps reaching a depth within $0.7 < \sigma_{1.1\,mm} < 2.8$ mJy, therefore ruling out any observational bias in our classification.

spectrum. The relatively fast internal switching ($\simeq 1$ kHz) between the RSR beams allows the minimization of the contribution from atmospheric noise into the ACF; nevertheless, small differences in the switching duty-cycle can introduce large baseline artifacts. To increase the detectability of spectral lines, the RSR_DRIVER can calculate and subtract a Savitzky–Golay filter (SGF) for each band,

analogous to performing a high-pass filter on the observed data.[3] The number of points used to simultaneously fit the filter determines its cut-off frequency. In this work, we used a length of 55 frequency channels to cut out all the features broader than $\simeq 1.71$ GHz ($\Delta V \simeq 5500$ km s^{-1}), which is much larger than the expected CO line widths from high-redshift SMGs. The RSR_DRIVER allows us to automatically remove noisy data from the spectrum. A typical 5 min integration yields a $\sigma_{T_{A^*}} \simeq 2$–4 mK. All bands with $\sigma_{T_{A^*}} > 5$ mK are therefore ignored by the pipeline. The construction of the final spectrum is achieved by a weighted average of all the observations available for an astronomical source. Fig. 5 shows one example of the resulting RSR spectrum and a comparison between the results obtained with the different baseline improvement techniques. It is important to notice that the output of the RSR_DRIVER wrapper produces a significant ($\times 1.5$) improvement on the line-peak SNR of the observed CO transitions, which would be important for the identification of fainter transitions with lower SNRs. This semi-automatic procedure provides an user-friendly tool to reduce RSR data in an homogeneous and efficient way.

3 ANALYSIS AND RESULTS

3.1 Source detection and flux measurement

3.1.1 Detection algorithm

Sources were identified using the AzTEC SNR map of each observation and adopting a SNR threshold. If a source is detected in a map, we measure the 1.1 mm flux density and noise at the position of the pixel with the maximum SNR value as well as its celestial coordinates. A mask of 1.5 times the size of the AzTEC beam ($\theta_{1.1\,mm} \approx 9.5$ arcsec) is applied to the source before repeating the process again until no more sources above our adopted threshold are detected in the map. This process is conducted within the 50 per cent coverage of the maximum depth, which corresponds to typical areas of 6.1–10.8 arcmin^2 per map.

A 4σ detection threshold was adopted to minimize the contamination from false detections due to the noise in the maps. False detection probabilities are estimated in three different ways. In method (a), the noise simulations generated by the AzTEC pipeline (jackknife maps) are used to identify positive noise peaks (i.e. the false detections), which are then divided by the number of detections in the real maps. In method (b), the number of false sources estimated above are divided by the expected number of sources in the map, which we calculate by adding the false sources to the number counts from blank fields (Scott et al. 2012) plus 1 (to compensate for the fact that we are targeting biased fields where we expect to find at least one source). Finally, in method (c) the number of negative peaks in the SNR map (representative of the noise in the map) are divided by the number of positive detections.

Fig. 6 shows the results of our FDR analysis and how, for our adopted search radius of $r = 36.6$ arcsec, the three methods converge at SNR $\gtrsim 4$, where the contamination due to false detections is $\lesssim 5$ per cent. This contamination drops to ~ 2 per cent for 4σ sources detected within the central and deeper $r = 15$ arcsec area of the maps, where the reliability of 3.5σ and 3σ detections increases to $\gtrsim 90$ per cent and 75 per cent, respectively.

---

[3]If the SGF is applied, the polynomial baseline subtraction from the previous step is not performed.

Table 2. Measured properties of the detected CO transitions in the 3 mm RSR spectra. The spectroscopic redshifts estimated in this work from the LMT/RSR spectra are given in column 7 and, for comparison, those previously published are listed in column 8.

ID	Transition	ν_{line} (GHz)	Peak flux (mJy)	Integrated flux (Jy km s^{-1})	FWHM (km s^{-1})	z_{spec} LMT/RSR	Literature
G09-81106	CO(4 − 3)	83.40 ± 0.01	2.50 ± 0.41	1.36 ± 0.17	727 ± 128	4.531 ± 0.006	4.531 ± 0.001[a]
	CO(5 − 4)	104.28 ± 0.02	4.06 ± 0.33	2.21 ± 0.32	899 ± 70		
G09-83808	CO(5 − 4)	82.03 ± 0.01	2.75 ± 0.29	1.27 ± 0.17	584 ± 120	6.026 ± 0.005	6.0269 ± 0.0006[b]
	CO(6 − 5)	98.41 ± 0.01	2.29 ± 0.41	0.90 ± 0.17	418 ± 115		
	H$_2$O(2_{11} − 2_{02})	106.99 ± 0.01	2.96 ± 0.48	0.79 ± 0.11	227 ± 49		
G12-26926	CO(4 − 3)[d]	79.93 ± 0.01	8.53 ± 0.45	1.98 ± 0.18	641 ± 38	4.768 ± 0.002[c]	
	CO(5 − 4)[d]	99.86 ± 0.01	4.58 ± 0.40	0.93 ± 0.22	520 ± 41		
NGP-203484	CO(4 − 3)	80.51 ± 0.01	5.39 ± 0.54	1.53 ± 0.25	376 ± 45	4.728 ± 0.002[c]	
	CO(5 − 4)	100.59 ± 0.01	7.03 ± 0.68	1.59 ± 0.17	243 ± 31		
NGP-246114	CO(4 − 3)	95.13 ± 0.03	2.05 ± 0.52	1.04 ± 0.13	476 ± 168	3.847 ± 0.002[e]	3.847 ± 0.002[a]
NGP-284357	CO(4 − 3)[d]	78.16 ± 0.01	8.83 ± 0.41	1.60 ± 0.21	626 ± 36	4.891 ± 0.006	4.894 ± 0.003[a]
	CO(5 − 4)	97.81 ± 0.01	3.31 ± 0.48	1.69 ± 0.22	535 ± 100		

[a] Fudamoto et al. (2017). [b] Zavala et al. (2018a) including an additional [C II] with SMA. [c] New LMT/RSR determinations derived in this work. [d] First published CO transitions using the 50 m-LMT. [e] Estimated including the CO(6 − 5) transition of Fudamoto et al. (2017).
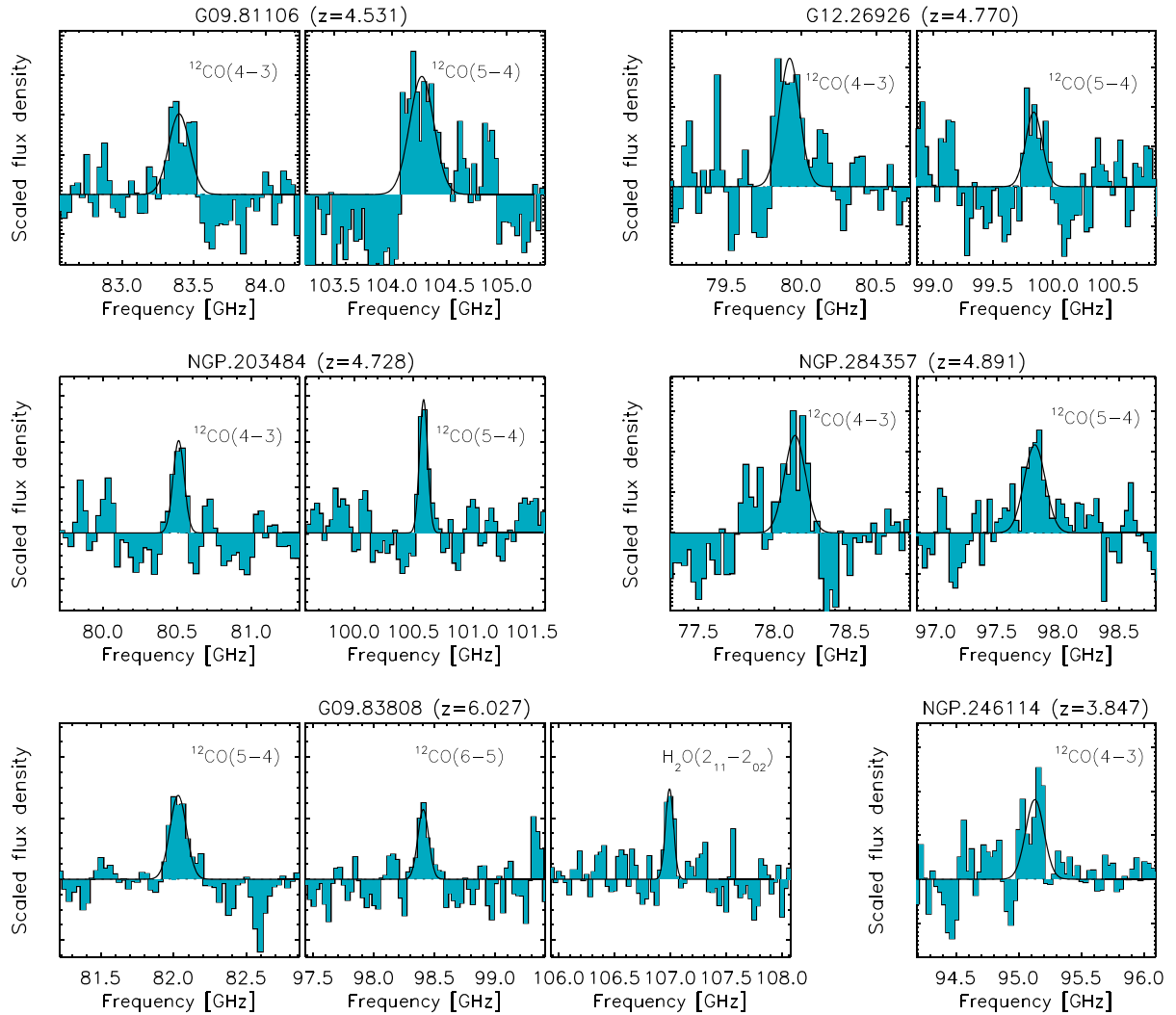
Figure 4. Identified lines in the RSR spectra along with the best-fitting Gaussian functions. The redshift of each source is identified on the top and the individual transitions are labelled close to the lines. Each panel has a total width of 6000 km s^{-1} and is centred on the central frequency of the respective line. The identified lines in G09.83808 are the same as in Zavala et al. (2018a). The fitted parameters to each line are listed in Table 2.
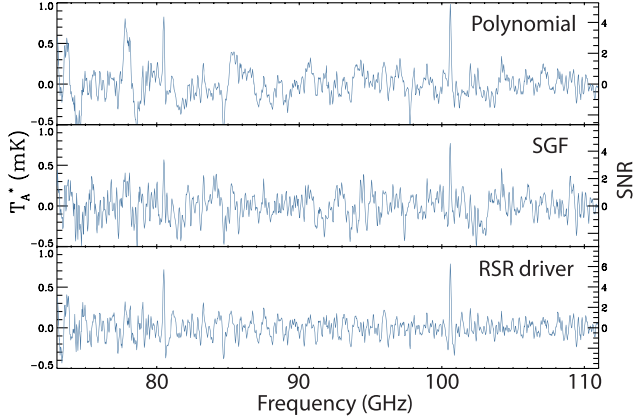
Figure 5. RSR spectra of source NGP-203484 ($z = 4.728$) obtained with the different baseline-subtraction techniques available within the pipeline. Top: the standard output of the DREAMPY package using a low-order polynomial baseline subtraction. Middle: the resulting spectrum by visually inspecting and removing the noisy data, and subtracting a SGF. Bottom: the output produced by the recently developed RSR_DRIVER, including both, a low-order polynomial baseline subtraction and a SGF. The output of the RSR_DRIVER wrapper produces a $\sim \times 1.5$ improvement on the line-peak SNR of the observed CO transitions.
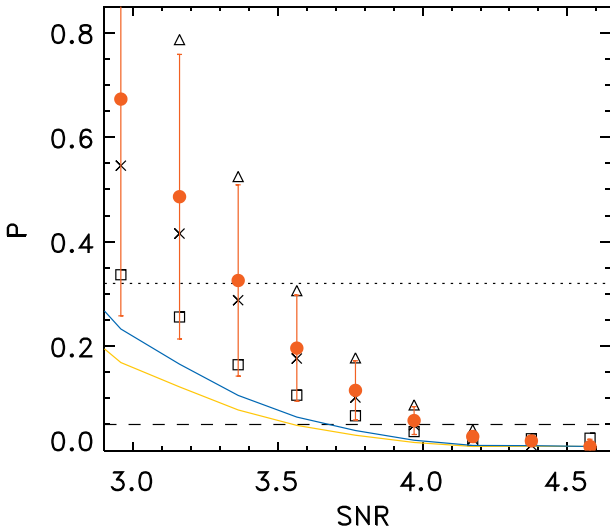
Figure 6. FDR (P) estimated within the adopted search area ($r = 36.6$ arcsec) as a function of SNR. Triangles, crosses, and squares correspond to methods (a), (b), and (c), respectively, to estimate the FDRs (see text). Filled red circles indicate the mean of the three methods. Dashed and dotted lines indicate 5 per cent and 32 per cent contamination, respectively. The blue and yellow curves correspond to the expected FDR for sources detected within the deeper central $r = 15$ and $r = 10$ arcsec region of the maps.

We have also estimated the completeness of our survey as a function of flux density by inserting synthetic sources (1000 sources per flux density bin) in the AzTEC maps and quantifying the recovery efficiency. The sources are inserted within the 85 per cent coverage region considered in our analysis. Nevertheless, if a source is detected within 5 arcsec from a real detection, it is excluded from the completeness calculation. Fig. 7 summarizes the completeness of our survey. Assuming typical SMG SED templates (e.g. Michałowski, Hjorth & Watson 2010; da Cunha et al. 2015b; or modified black-bodies with $T_{dust} = 40$–50 K and $\beta = 1$–2) at $z \geq 3$, scaled to the
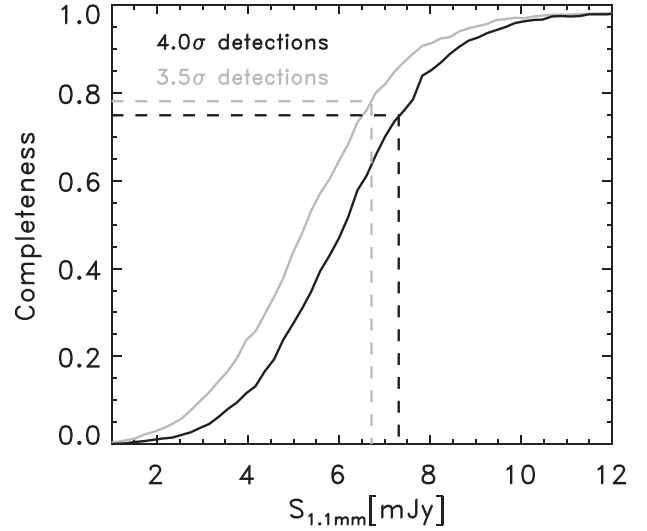

Figure 7. Completeness fraction as a function of 1.1 mm flux density for our AzTEC survey of red-*Herschel* targets, estimated by inserting synthetic sources in different flux density bins and attempting to recover them above a 4.0σ (black) and 3.5σ (grey) detection threshold. If we extrapolate the 500 μm flux density using typical SMG SED templates (e.g. Michałowski et al. 2010; da Cunha et al. 2015b; or modified black bodies with $T_{dust} = 40 - 50$ K and $\beta = 1 - 2$) at $z = 3$, the expected median 1.1 mm flux densities are $\gtrsim 9$ mJy, corresponding to a completeness $\gtrsim 90$ per cent. The median flux density of the AzTEC detections, however, suggests a more conservative ~ 75 per cent completeness (dashed lines).

average 500 μm flux density of our red-*Herschel* targets, we infer a completeness $\gtrsim 90$ per cent given the expected 1.1 mm flux densities $\gtrsim 9$ mJy. Nevertheless, the median flux density of our AzTEC 4σ detections of $S_{1.1mm} = 7$ mJy (see below) suggests a lower completeness of around 75 per cent, which should be considered more reliable.

The same set of simulations are then used to explore the impact of flux boosting, meaning sources' flux densities systematically biased upwards by noise and the presence of unresolved astronomical sources below the detection threshold. Given the relatively low number of sources at the depth of our observations (around 0.006 sources per AzTEC beam at our typical 1σ RMS depth), we infer an average flux boosting factor of ~ 1.15 for those sources detected at our detection threshold of SNR $= 4$. The average flux boosting decreases with flux density (or similarly with SNR) and it is almost negligible at SNR $\gtrsim 5.5$.[4] This value is not taken into account given the relatively larger uncertainties of the sources' flux densities (25 per cent for a source detected at SNR $= 4$).

In the 93 analysed maps, we find a total of 79 AzTEC detections above our adopted threshold (SNR > 4) within the 50 per cent coverage area. The counterpart matching between the *Herschel* and these AzTEC sources was then performed using the 500 μm *Herschel* beamsize as a reference. An AzTEC source is associated with a *Herschel* source if its AzTEC position lies within $\theta_{500\,\mu m} = 36.6$ arcsec of the *Herschel* position (although most of

[4]Note that our observations are far from being confusion noise limited. Assuming the most recent 1.1 mm number counts from Zavala et al. (2021) and defining confusion noise at the level of 1/30 source per beam, we estimate the confusion noise to be around 0.35 mJy for the 32-m LMT, which is a factor of ≈ 4–$6 \times$ deeper than the typical noise in our observations.
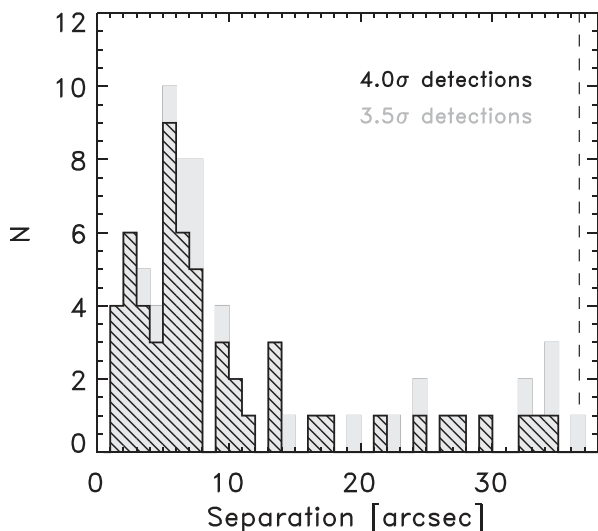
Figure 8. Histogram of the separations between the AzTEC detection and *H*-ATLAS targeted positions. Although a radius $\theta_{500\,\mu m} = 36.6$ arcsec (vertical dashed line) is used for our counterpart analysis, $\sim$82 per cent (75 per cent) of the 4σ (3.5σ) AzTEC sources are separated by $\lesssim 15$ arcsec off the *H*-ATLAS target, were the reliability of the detections is $\gtrsim 98$ per cent (90 per cent; see Fig. 6).

them lie within ~ 15 arcsec; see Fig. 8). Out of the 93 red-*Herschel* targets, 40 are associated with individual AzTEC sources, while eight break into multiple AzTEC components (comprising a total of 16 AzTEC detections) and therefore are classified as multiple systems (see Section 3.3). This leaves 45 *Herschel* targets with no AzTEC detections at the $>4\sigma$ level, which are discussed in Section 3.2.

3.1.2 Serendipitous sources

Additionally, we find 23 AzTEC 'serendipitous' detections that lie outside the adopted search radius, i.e. they are not directly associated with any red-*Herschel* source in the sample and do not contribute to the *Herschel*-500 μm flux density. Given the total mapped area ($\sim$720 square arcmin without considering the central regions of the maps) and the flux detection threshold assumed in our analysis ($S_{1.1mm} \gtrsim 8$ mJy in the outer region of the maps), the number of serendipitous detections (23) is much larger than the number of sources ($\sim$4) predicted from AzTEC blank-field number counts (Scott et al. 2012). The probability of finding this number of serendipitous sources within the mapped area by chance is $\sim 8 \times 10^{-12}$. Furthermore, moderate resolution single-dish number counts as those reported in Scott et al. (2012) are known to over-estimate the number of bright sources due to source blending (e.g. Lindner et al. 2011; Karim et al. 2013; Béthermin et al. 2017; Stach et al. 2018). Taking this into account would further increase the discrepancy we report.

The estimated overdensity parameter of 4.75 ($\delta(> S) \equiv N(> S)/N(> S)_{\text{blankfield}} - 1 = 4.75$) is conservative since we are excluding all sources within the multiplicity search radius (i.e. $r = 36.6$ arcsec). It is also consistent with the results of Lewis et al. (2018) from LABOCA 870 μm follow-up observations of 22 ultra-red *Herschel* sources, who found $\delta(> S_{870\,\mu m}) \sim 4$–30 for $S_{870\,\mu m} \sim 13$–16 mJy (i.e. equivalent to our 4σ detection threshold of $S_{1.1\,mm} \gtrsim 8$ mJy). This excess suggests that some of these red-*Herschel* sources are associated with galaxy overdensities. This deserves further analysis

which is beyond the scope of this work; therefore, these serendipitous sources are not discussed in the rest of the paper since they are not directly associated with the originally targeted red-*Herschel* sources.

3.1.3 Deblending Herschel observations

We estimate deblended flux densities in the *Herschel* bands for all the AzTEC detections in a similar way to that presented in Michałowski et al. (2017, see details of the method therein). Briefly, we extract a square 120 arcsec wide around the position of a given AzTEC source and simultaneously fit 2D Gaussian functions at the positions of all AzTEC sources within this square patch (the fitting is performed using the IDL MPFIT package, Markwardt 2009). The normalization of each Gaussian function is kept as a free parameter, whereas its FWHM is fixed at the size of the respective *Herschel* beam. The errors on the deblended flux densities are calculated from the covariance matrix in order to take into account the possible degeneracies in the fitting. This is especially important for close sources that lie within the beam at a given band, whose fluxes are highly degenerate. The confusion limit of the SPIRE data, reported as 5.8, 6.3, and 6.8 mJy beam^{-1} at 250, 350, and 500 μm (Nguyen et al. 2010), are also added in quadrature. The AzTEC 1.1 mm flux densities and the deblended *Herschel* flux densities derived in this work are reported in Table A1.

3.2 On the nature of non-detections

After performing the counterpart matching, 45 of the 93 analyzed red-*Herschel* targets do not have an associated AzTEC detection at $\geq 4\sigma$ significance within 36.6 arcsec. Since the incompleteness of our survey can not explain the bulk of these non-detections (see Section 3.1), here we explore four possible scenarios to explain them: (1) AzTEC observations do not reach the desired sensitivity; (2) these targets correspond to the faintest *Herschel* sources and thus deeper observations are needed; (3) these sources are made up of multiple intrinsically fainter components blended within the *Herschel* beam; and (4) the sources show different SED properties.

As shown in Fig. 3, in general, the AzTEC observations on these non-detected targets have a similar rms noise as those in which sources were detected (see yellow histogram in the figure). This confirms the homogeneity of our observations, ruling out the first scenario discussed above. Similarly, these AzTEC non-detections have similar *Herschel* flux densities to the detected galaxies (Fig. 2), spanning a flux density range of $S_{500\mu m} \approx 40 - 80$ mJy. Therefore, if those were single sources with SEDs similar to those of the detected galaxies, we would expect most of them to be detected above the adopted threshold, although a small fraction of them could be associated to the faintest sources. Actually, looking at the AzTEC maps individually, we find 8 (15) sources at SNR ≥ 3.5 (3.0) close to the *Herschel* position (at $r \lesssim 10$ arcsec), which are consistent with being single systems but falling below our detection threshold (SNR = 4). Note that the reliability of these 3.5σ and 3σ detections is $\gtrsim 93$ per cent and $\gtrsim 80$ per cent, respectively (see FDR for the central $r = 10$ arcsec radius region in Fig. 6), which suggest that these single faint sources are real.

Considering that the percentage of spurious detections in the *H*-ATLAS catalogues is reported to be $\simeq 0.2$ per cent[5] (Valiante et al.

---

[5]Given the complex selection process of our sample (see Section 2.1), the FDR may be >0.2 per cent. Nevertheless, we do not expect it to be large enough to justify all the AzTEC non detections, since all of our *Herschel*

2016), the remaining non-detections are therefore likely multiple systems with individual members' flux densities below our sensitivity limit or sources with different SED properties. In fact, Valiante et al. (2016) explicitly suggest that 'a more important problem than spurious sources is likely to be sources that are actually multiple sources'. After visual inspection, we identify at least nine systems with multiple components at SNR > 3.5, suggesting that multiplicity is indeed a main reason for the non-detection of these galaxies.

However, although there are no significant differences between the *Herschel* colours of the detected and the non-detected systems (see Fig. 1), suggesting similar SED shapes, we cannot rule out the possibility that some of the non-detected sources have a higher dust emissivity spectral index, β. This would also decrease the expected flux density in the Rayleigh–Jeans regime probed by the AzTEC 1.1 mm observations, potentially explaining the lack of detections in some of these targets. In fact, the median 1.1 mm flux density of the AzTEC detections seems a bit lower than what it is predicted by using typical SED templates (e.g. Michałowski et al. 2010; da Cunha et al. 2015a; see also Section 3.1). This might be in line with recent results reporting steeper β values in $z > 3$ galaxies (e.g. Kato et al. 2018; Jin et al. 2019; Casey et al. in preparation), suggesting an evolution of the dust emissivity index with redshift and/or luminosity.
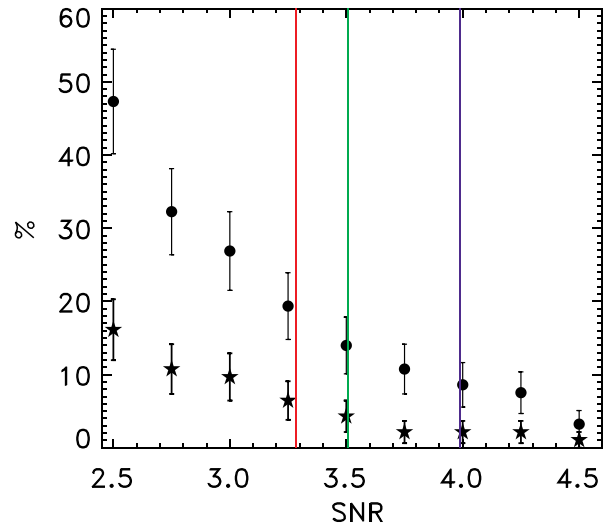
3.3 Multiplicity fraction

Our observations are sensitive to galaxies separated by $\Delta\theta >$ 9.5 arcsec. Sources with such separation are hard to detect in the small field of view of interferometric observations as those achieved with ALMA[6] and NOEMA. Indeed, Ma et al. (2019) noted that, for some of their red-*Herschel* sources, the total flux densities measured by ALMA are systematically lower than those measured with single-dish telescopes, suggesting the presence of multiple components beyond their mapped area. Our observations thus probe multiplicity at a different scale from what has been studied so far with interferometers.[7]

Using our search radius of 36.6 arcsec (the size of the *Herschel* beam at 500 μm), we find that eight targets from the original sample show source multiplicity, comprising a total of 16 AzTEC detections. This implies that at least ~9 per cent (8/93) of the red-*Herschel* targets with AzTEC detections are composed of multiple systems. Additionally, nine of the non-detections are likely multiple systems made of intrinsically fainter galaxies with individual flux densities falling just below our detection threshold (see Section 3.2). Further- more, four of the targets originally classified as single detections correspond to multiple systems if the detection threshold is reduced to include $\geq 3.5\sigma$ sources. These additional sources lie within the central ($r \lesssim 15$ arcsec) deeper region of the maps, where the reliability of 3.5σ detections is >90 per cent. Including these, the multiplicity fraction is increased to ~23 per cent (21/93). An extreme scenario would be if all of the AzTEC non-detections are also assumed to be multiple systems. In that case, the multiplicity fraction of the red *Herschel* sources would be as high as 50 per cent. Fig. 9 shows, for

---

sources were identified in the 250 and 350μm maps, and detected above 5σ at 500 μm.

[6]The ALMA primary beam at 850 μm has a half power beamwidth of 18 arcsec. Hence, at a radius larger than ~9 arcsec, the primary beam response drops below 0.5.

[7]We note that the field of view of the SMA can probe angular scales < 27 arcsec (ignoring the drop in efficiency towards the edge of the beam). The relatively small samples observed so far, however, have limited the detection of systems separated by these larger angular scales.

Figure 9. Multiplicity fraction as a function of signal to noise detection threshold, and for two search radii: 36.6 arcsec (circles) and 18.3 arcsec (stars). Error bars correspond to $\sqrt{N}$. Vertical lines indicate false detection contamination of 5 per cent (dark blue at SNR ~4), 20 per cent (green at SNR ~3.5), and 32 per cent (red at SNR ~3.3), estimated within the central $r = 36.6$ arcsec area of the AzTEC maps.

two different search radii, how the multiplicity fraction increases as the detection threshold in our analysis is reduced.

The multiple fraction may be even larger if multiplicity at smaller scales than the AzTEC beam is also present within the sources classified here as single systems.

To probe the multiplicity at smaller scales, we perform two different tests in which the measured PSF profile of single sources is comparable to that of an expected point source. Deviation on the width and shape of the PSF would be expected if two or more sources are blended within the AzTEC beam. First, we derive a radial profile for each detection by azimuthally averaging its flux density and compare its FWHM against that of the point-source PSF. Secondly, for each AzTEC source, we subtract the point-source PSF scaled to the corresponding measured flux value and quantify the residuals within a $1.5 \times$ FWHM area. Then, those sources with broad FWHMs ($\gtrsim 10$ per cent than the ideal PSF – i.e. $\sim 2\sigma_{PSF}$ the standard deviation of the PSFs in our sample) and/or with residuals larger than the noise level are tagged as potential close multiples. Based on this analysis, we expect multiplicity in $21-33$ per cent of the AzTEC detections classified as singles.

These estimations can be compared to the results from inter- ferometric observations on samples of red-*Herschel* sources. For example, Ma et al. (2019) reported that ~27 of a compilation of 63 red-*Herschel* galaxies observed with ALMA, NOEMA, and the SMA are close multiple systems. Greenslade et al. (2020) have also recently reported 870 μm and 1.1 mm SMA observation of 34 red 500 μm-risers from the *Herschel* Multitiered Extragalactic Survey (Oliver et al. 2012), and find a ~12 per cent multiplicity fraction. However, they argue that their 12 non-detections are most likely multiple systems with more than two members, in which case their multiplicity fraction increases to 47 per cent.

Our estimates of the fraction of close multiple systems are in broad agreement with the literature, implying that the multiplicity fraction of the whole sample might be larger than the values reported above when accounting for the multiplicity at smaller

scales than the AzTEC beam. Nevertheless, combining these higher-resolution interferometric results with our multiplicity estimations is not straightforward. A careful visual inspection of the 63 red-*Herschel* sources presented in Ma et al. (2019) indicates that 14 of them (∼ 22 per cent) are multiples at scales below those probed by our AzTEC observations, and would therefore be classified as individual systems in our analysis. This implies that our multiplicity estimates should be increased by an additional ∼10 per cent due to multiple systems that are not resolved within the AzTEC beam. The resulting total multiplicity fraction of red-*Herschel* sources would therefore be ≳18 per cent in the conservative scenario and ∼60 per cent in the extreme one, in which most of the non-detections are also considered to be multiples.

Similar results are found if we instead adopt the results from our PSF modelling analysis, but the reader should keep in mind that different factors other than multiplicity (e.g. focus and astigmatism of the telescope, noise gradient in the maps, or even strong gravitational lensing effects) could distort and broaden the shape of the AzTEC beam. Therefore, we stress that follow-up higher angular resolution observations are necessary to derive a robust estimation of the total multiplicity fraction in our sample.

3.4 Redshifts and luminosities

In order to estimate photometric redshifts, luminosities, and SFRs, we follow the procedure described in Ivison et al. (2016), in which a library of template SEDs is adopted in order to better characterize the diversity of the intrinsic SEDs and the uncertainties in the derived quantities. We use four SEDs which are representative of DSFGs, and particularly, of red-*Herschel* sources (see Ivison et al. 2016). This set includes Arp220 (Silva et al. 1998), the Cosmic Eyelash (Swinbank et al. 2010; Ivison et al. 2010), and the two synthesized templates of Pope et al. (2008) and da Cunha et al. (2015b).

Our SED fitting approach is based on a maximum-likelihood method which formally takes into account upper limits in case of non-detections (e.g. Aretxaga et al. 2007; Sawicki 2012). This is important since the *Herschel* flux densities of some of the sources lie below 2.5σ after using the AzTEC positions as priors to deblend the *Herschel* emission (see Section 3.1). We test our procedure combining the AzTEC photometry (including an additional 5 per cent calibration uncertainty) with all the *Herschel* data (PACS 100 and 160 μm and, SPIRE 250, 350, and 500 μm), with only PACS 160 μm plus all the SPIRE bands, and with only SPIRE photometry. Given the typical low SNR of PACS 100 μm (plus the possible contribution from emission mechanisms not included in the adopted SED templates – e.g. AGN, PAHs, etc.), the best fits are achieved when using only PACS 160 μm in combination with the SPIRE and AzTEC photometry. We therefore discard the 100 μm band during the SED fitting procedure.

For each source in our catalogue, a redshift probability distribution is calculated by combining the redshift distributions associated with the four different SED templates described above. Then, the best-fitting photometric redshift is assumed to be the one with the maximum likelihood, and the 68 per cent confidence interval is estimated by integrating the combined redshift distribution. As shown in Fig. 10, the photometric redshifts derived by this method, which are reported in Table A1, are in good agreement with those reported in the literature (Ivison et al. 2016; Fudamoto et al. 2017; Duivenvoorden et al. 2018; Zavala et al. 2018a; Ma et al. 2019); with eight being spectroscopic redshifts). The relative difference between our redshifts and those derived elsewhere is estimated to be $\Delta z/(1 + z_{ref}) = 0.10$ and 0.09 if only the spectroscopic redshifts are
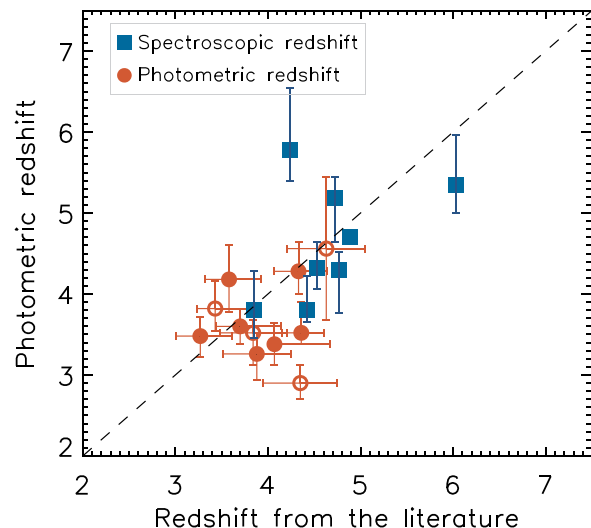

Figure 10. Comparison between the photometric redshifts derived in this work and those reported in the literature (Ivison et al. 2016; Fudamoto et al. 2017; Duivenvoorden et al. 2018; Zavala et al. 2018a; Ma et al. 2019), including both photometric (orange circles) and spectroscopic redshifts (blue squares; see Table 2 and Section 4.1). The open circles represent sources which are classified as multiple systems based on our AzTEC observations, while all the remaining sources correspond to single systems. In general, our estimated redshifts are in good agreement with those reported in the literature with a mean redshift deviation of $\Delta z/(1 + z_{ref}) = 0.09$ (considering only those sources with spectroscopic redshifts).

considered. These values are similar to the expected uncertainties for photometric redshifts (Hughes et al. 2002). Additionally, we estimate the photometric redshifts with the MMPZ code (Casey 2020) and find consistent results (with a mean difference of $\Delta z/(1 + z_{ref}) = 0.004$ for the single sources), although with significantly larger uncertainties.

Fig. 11 shows the stacked probability redshift distribution of all the AzTEC-detected red-*Herschel* sources, which has a median redshift of $z_{med} \approx 3.64$. We also plot the stacked redshift distribution of the single and multiple systems separately. Although both distributions have similar median redshifts ($z_{med} \approx 3.8$ *versus* 3.5), the multiple systems have a larger fraction of low-redshift sources (27 per cent at $z_{phot} < 3$) compared to the single systems (10 per cent). We highlight that, although only ∼33 per cent of the total redshift distribution lie at $z_{phot} > 4$, the adopted colour selection criteria is efficient at selecting $z_{phot} > 3$ galaxies, where ∼85 per cent of the sample lie. In Fig. 11, we also compare the redshift distribution of the AzTEC-*Herschel* sources with those from similar samples derived in Duivenvoorden et al. (2018) and Ma et al. (2019), which have median photometric redshifts of 3.6 and 3.3, respectively. Similarly, Ivison et al. (2016) reported a median redshift of 3.66, with ∼32 per cent of the sources lying at $z > 4$. Our results are therefore in general agreement with those previously reported.

The IR luminosity is then derived using the best-fitting template and integrating from $8 - 1000$ μm (in the rest frame), from which the SFR is estimated assuming the Kennicutt & Evans (2012) calibration for a Chabrier (2003) IMF, SFR $[M_\odot \text{ yr}^{-1}] = 1.48 \times 10^{-10} L_{IR} [L_\odot]$. The uncertainties on the infrared luminosities (and hence SFRs) are propagated from the flux density and redshift errors using Monte Carlo simulations. The estimated IR luminosities and SFRs can be found in Table A1.

Fig. 12 shows the IR luminosity and SFR histogram of our AzTEC sources, which have apparent IR luminosities in the range of 12.8
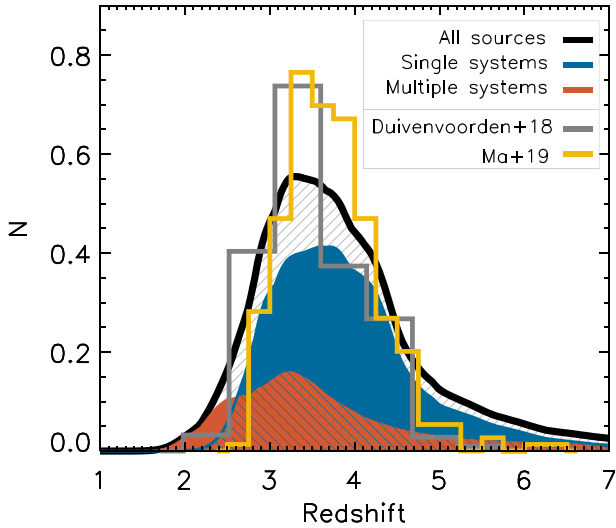
Figure 11. Normalized redshift distribution of the AzTEC-detected red-*Herschel* sources derived from the stacking of the redshift probability distribution functions. The components of multiple systems are represented by the orange distribution while the single systems are illustrated by the blue distribution. Although both redshift distributions have a similar median value, that for multiple systems is more skewed towards lower redshifts. The redshift distribution of all the sources is plotted as the black solid curve. For comparison, previous estimations of similar red samples are also included (Duivenvoorden et al. 2018; Ma et al. 2019).
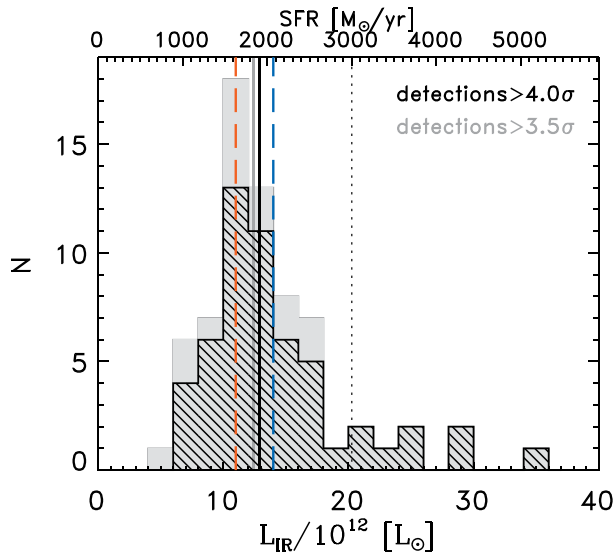
Figure 12. Histogram of IR luminosities and SFRs estimated for the AzTEC detections above 4σ (black line filled) and 3.5σ (light grey). The median values of both distributions are indicated with vertical lines, including the median luminosity for the 4σ single systems ($1.4 \times 10^{13} L_\odot$; dashed blue) and the components of the multiple systems ($1.1 \times 10^{13} L_\odot$; dashed orange). Eight sources in our sample show $L_{IR} > 2 \times 10^{13} L_\odot$ and SFRs $>3000\,M_\odot\,yr^{-1}$ (dotted vertical line), representing a population of extreme star-forming galaxies that cannot be explained within current physically plausible models, unless gravitational lensing effects are included.

$\leq \log_{10}(L_{IR}/L_\odot) \leq 13.5$, with a median luminosity of $1.4 \times 10^{13} L_\odot$ for the single systems and $1.1 \times 10^{13} L_\odot$ for the components of the multiple systems. Their SFRs span $\sim900\,M_\odot\,yr^{-1}$ to $5000\,M_\odot\,yr^{-1}$, representing some of the most extreme star-forming galaxies known (in the absence of gravitational lensing). These values are in good agreement with those reported in the literature for similar samples. For example, Ivison et al. (2016) reported apparent luminosities in the range of $5 \times 10^{12} - 6 \times 10^{13} L_\odot$ with a median of $1.3 \times 10^{13} L_\odot$, Ma et al. (2019) derived a median luminosity of $9.0 \times 10^{12} L_\odot$, and Greenslade et al. (2020) report luminosities in the range of $2 \times 10^{13} - 6 \times 10^{13} L_\odot$. These values are also comparable to those estimated for the sample of DSFGs selected with the *SPT*, which have a median intrinsic luminosity of $L_{IR} \approx 1.5 \times 10^{13} L_\odot$ (Reuter et al. 2020).

4 IDENTIFICATION OF INTERESTING SUB-SAMPLES

4.1 High-redshift galaxy candidates

To isolate the most promising high-redshift galaxies, we select all those *Herschel*-AzTEC systems detected above the 4σ threshold and with $z_{phot} > 4$. The 18 sources which satisfy this criterion are identified in Table A1, three of which are members of multiple systems. Their photometric redshifts span $z = 4.0$ to ~5.8 and have SFRs in the range of $\approx1000-5000\,M_\odot\,yr^{-1}$, representing some of the most luminous DSFGs known so far (in the absence of gravitational amplification).

Six of these candidates have already been spectroscopically confirmed at $z > 4$: SGP-272197 at $z = 4.24$ (source SGP-261206 in Fudamoto et al. 2017) and five of the sources in Table 2. Interestingly, G09-838083 ($z = 6.03$) was found to be gravitationally lensed by a foreground elliptical galaxy, with a magnification factor of ≈9.3 (Zavala et al. 2018a). This implies that, although the sources were selected to be preferentially non-lensed (see Section 2), there might be other amplified galaxies in the sample, and therefore, the SFRs quoted above would represent upper limits.

Regardless of their potential gravitational lensing amplification, these sources are ideal targets for future spectroscopic surveys aimed at identifying and characterizing dusty starburst galaxies in the early Universe.

Ivison et al. (2016) developed robust simulations to estimate the different completeness factors affecting the selection of the ultrared *Herschel* sample. Given the similar selection criteria between samples, we update their completeness estimates considering the $500\,\mu m$ flux density limit of our sample ($S_{500\,\mu m} \gtrsim 35$ mJy) and the number of sources in our analysis (93). Using this completeness correction, and considering the number of $z_{phot} > 4$ from our analysis, we estimate a lower limit for the space density of $4 < z < 6$ red DSFGs of $\approx 3 \times 10^{-7}$ Mpc^{-3}. This is a factor of two lower than that found by Ivison et al. (2016). However, Ivison et al. assumed a SNR detection threshold ≥2.5 for their SCUBA-2/LABOCA observations (FWHM ~18.4 arcsec), and did not consider potential multiplicity effects.

Combining our estimated space density and the median SFR of our $z_{phot} > 4$ sample ($\sim 2500\,M_\odot\,yr^{-1}$ not corrected for potential gravitational lensing effects), we conclude that luminous red *Herschel* sources contribute $\gtrsim 8 \times 10^{-4}\,M_\odot\,yr^{-1}$ Mpc^{-3} to the obscured star formation at $4 < z < 6$. This value is in very good agreement with the recent estimations of the dust-obscured SFR density presented by Zavala et al. (2021) based on ALMA

number counts at 1.2, 2, and 3 mm. Their model predicts a dust-obscured SFR density of $\approx 10^{+5}_{-6} \times 10^{-4}\,M_\odot\,yr^{-1}\,Mpc^{-3}$ at $z = 5$ from galaxies with IR luminosities in the range of our sources ($12.8 \leq \log_{10}(L_{IR}/L_\odot) \leq 13.5$).

4.2 Physically interacting galaxies

With redshifts in hand, we can speculate the nature of the multiple systems in our sample. Are they chance projections at different redshifts (e.g. Zavala et al. 2015) or physically interacting galaxies (e.g. Oteo et al. 2016)? Examples of both systems have been reported in the literature and, indeed, it is likely that these multiple systems are composed by both physically associated galaxies and chance projections (e.g. Hayward et al. 2018; Stach et al. 2018; Wardlow et al. 2018).

As discussed in Section 3.3, we are only sensitive to sources separated by $\Delta\theta \gtrsim 9.5$ arcsec (which corresponds to $\Delta \gtrsim 70$ kpc at $z = 4$). This prevents us from detecting late-stage mergers as those already identified by ALMA and the SMA (e.g. Oteo et al. 2016). Nevertheless, our observations enables the detection of pre-coalescence galaxy pairs and proto-cluster structures, whose identification by interferometers with small fields of view like ALMA or NOEMA is rather challenging. Such complexes represent ideal laboratories to study the environmental effects on the star formation activity and to understand the star formation process during the earliest stages of galaxy mergers.

To identify the most promising physically interacting systems, we select those multiple galaxies with photometric redshift consistent with each other within $\Delta z < 0.5$, since the typical photometric redshift uncertainty from SED-fitting methods is $\approx 0.2-0.3$ (Table A1; see also Aretxaga, Hughes & Dunlop 2005). Although this threshold might appear too relaxed, we highlight that the probability of finding a pair of two bright sources ($S_{1.1mm} \gtrsim 5$ mJy) by chance line-of-sight alignment is very low since their surface density is estimated to be around 0.01 arcmin^{-2} (Scott et al. 2012).

Out of the eight original targets that show multiplicity, only two fulfill this criterion. Two additional systems are identified if the detection threshold is reduced to 3.5σ. These sources are shown in Fig. 13 and are also identified in Table A1. As can be seen in the figure, some of these physically interacting candidates are well resolved into two separated sources. For three of these four systems, their redshifts agree within $\Delta z \lesssim 0.06$.

Although further observations are needed to confirm their nature, they might represent observational evidence of the existence of early-stage (pre-coalescence) mergers within the SMG population since their angular separations ($\approx 20-30$ arcsec or $\approx 150-200$ kpc) and their flux ratios (1:2) are in very good agreement with the predictions from simulations (e.g. Narayanan et al. 2010; Hayward et al. 2012).

5 DISCUSSION AND CONCLUSIONS

As part of the Early Science Phase of the Large Millimeter Telescope, we obtained AzTEC 1.1 mm observations on a sample of 100 red-*Herschel* sources. Their red far-infrared colours ($S_{250\,\mu m} < S_{350\,\mu m} < S_{500\,\mu m}$) and bright flux densities ($S_{500\,\mu m} \approx 35-80$ mJy) suggest that they are high SFR galaxies (SFRs $\gtrsim 500\,M_\odot\,yr^{-1}$) at high redshifts ($z \gtrsim 3$).

Combining the AzTEC data with our new deblended *Herschel* photometry, we constrained the multiplicity fraction in the sample and derived photometric redshifts, IR luminosities, and SFRs for all the sources in the catalogue. Our main results are discussed below and are also summarized in Fig. 14.
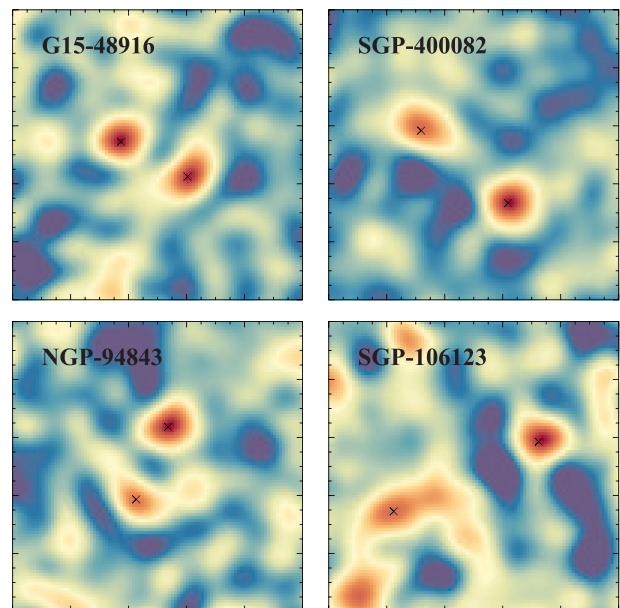

Figure 13. 76×76 arcsec^2 AzTEC 1.1 mm SNR maps of the four most likely physically interacting galaxy candidates in the sample. All the detected sources fall within 36.6 arcsec of the original *Herschel* position (the beamsize at 500 μm) and have individual photometric redshifts in agreement with each other within the error bars. These sources, which are typically missed in intereferometric observations due to their small fields of view, are likely galaxy over-densities and/or pre-coalescence galaxy mergers.
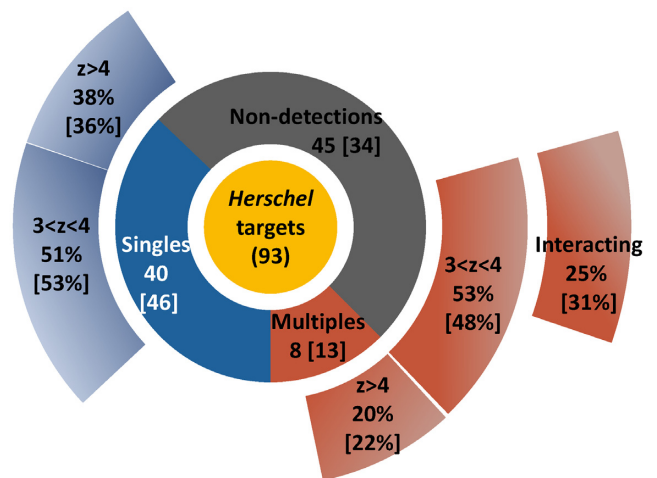
Figure 14. Summary of the results derived from the LMT/AzTEC observations. From the 93 observed red-*Herschel* targets, and assuming a 4σ (3.5σ) AzTEC detection threshold, 40 (46) were associated with single detections, 8 (13) with multiple sources, and 45 (34) with non-detections, within a search radius of 36.6 arcsec. These non-detected galaxies are also likely multiple systems, although some of them might be explained by having steep Rayleigh–Jeans slopes (see Section 3.2). From the detected galaxies, around 85 per cent of all the AzTEC-*Herschel* sources lie at $z_{phot} > 3$, while only 33 per cent at $z_{phot} > 4$. From the 8 (13) multiple systems, ~ 25 per cent (~ 31 per cent) are consistent with being physically associated galaxies ($\Delta z_{phot} \lesssim 0.5$), all of them lying at $z_{phot} \gtrsim 3$. The most promising $z > 4$ single sources and the physically interacting galaxy candidates are identified in Table A1.
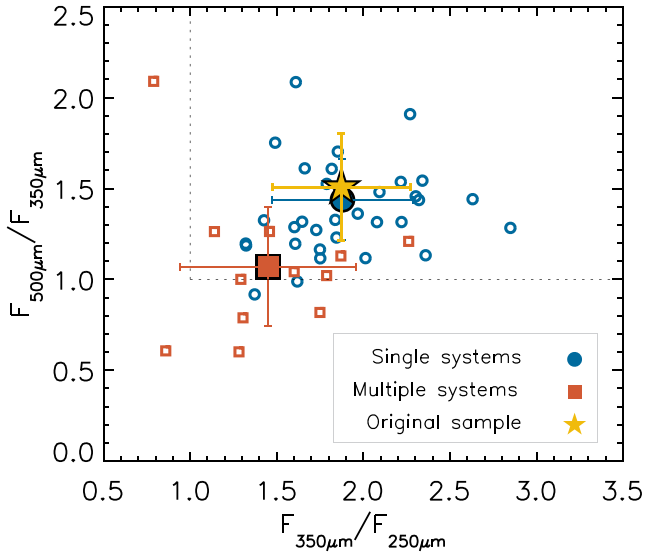
Figure 15. FIR colour-colour plot showing the singles (blue empty circles) and the components of multiple systems (orange empty squares) after deblending the *Herschel* fluxes using the detected AzTEC positions as priors. The solid blue circle and orange square indicate the average value of the corresponding samples, which have slightly different colours, with the multiple systems showing the least 'red' colours. Those sources with upper limits in any of the three bands are not plotted. For comparison, the average colour of the whole sample before deblending the fluxes is marked with a yellow star.

Thanks to the $\theta_{\mathrm{FWHM}} \approx 9.5$ arcsec angular resolution provided by the 32 m illuminated surface of the LMT (a factor of 4 better than *Herschel* at 500 μm), we found that eight of the red-*Herschel* targets break into multiple components (with SNR ≥ 4), which implies a multiplicity fraction of ~ 9 per cent. This value increases to ~ 23 per cent if we include those sources with evidence of multiplicity but slightly below our detection threshold (i.e. formally classified as non-detections). The multiplicity fraction can be even higher (up to ~ 50 per cent) if some of the non-detected sources were also made of multiple systems[8] (see Section 3.3). These multiple sources probe a different scale from what has been studied so far with smaller field of view interferometric observations. Hence, the multiplicity fraction quoted above might be larger if multiplicity at smaller scales (e.g. Ma et al. 2019; Greenslade et al. 2020) is also present within the sources classified here as single systems.

Such high multiplicity should be taken into account when comparing the properties of these galaxies to results from theoretical models and simulations, particularly since source blending artificially increases the redness of the colour in the *Herschel* bands due to the larger beamsizes of the redder filters. This can be seen in Fig. 15, where the FIR colours of the single and multiple systems are plotted after deblending the *Herschel* flux densities (blue circles and orange squares, respectively), along with the average colour of the whole sample before deblending the fluxes (yellow star). In general, the multiple systems have individual colours which are less red than those of the single systems and the average original colour used for the selection of these galaxies. Indeed, as seen in Table A1,

---

[8]Note, however, that we cannot rule out the possibility that some of the non-detected sources might have a higher dust emissivity spectral index, β, which would decrease the expected flux density in the Rayleigh–Jeans regime probed by the AzTEC 1.1 mm observations.
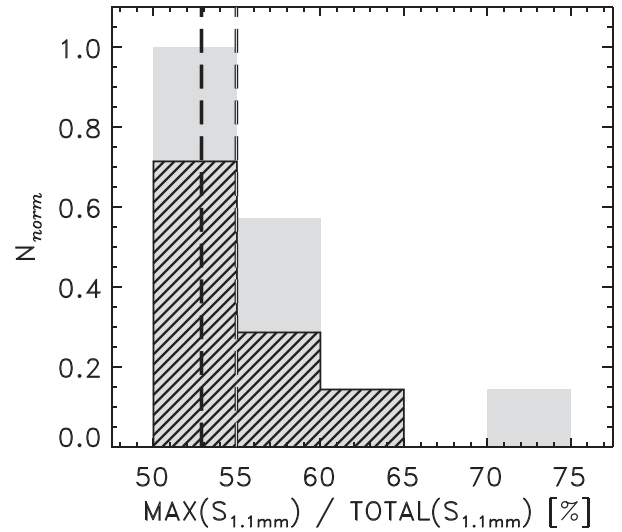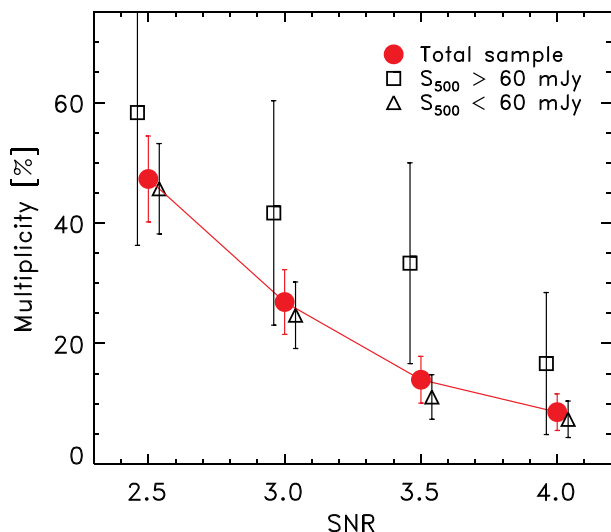

Figure 16. Normalized distribution of the AzTEC 1.1 mm flux density ratio between the brightest source of the multiple systems with respect to the total flux density of the system. Solid-grey and line-filled histograms correspond to a $3.5\sigma_{1.1\,\mathrm{mm}}$ and $4.0\sigma_{1.1\,\mathrm{mm}}$ detection thresholds, respectively. Vertical dashed lines indicate the median value for each distribution. Histograms have been normalized to the peak value of the $3.5\sigma_{1.1\,\mathrm{mm}}$ distribution.

14 of the 56 AzTEC detections associated with *Herschel* sources (~ 25 per cent) do not fulfill the condition $F_{250\mu m} < F_{350\mu m} < F_{500\mu m}$ after the deblending of the *Herschel* fluxes,[9] and 23 (~ 41 per cent) would be excluded after our colour cut ($S_{500\mu m}/S_{250\mu m} > 2$ and $S_{500\mu m}/S_{350\mu m} > 1$; see Section 2). This is in line with Ma et al. (2019), who suggest that ~ 20 per cent of their sources would not pass the selection criteria of 500 μm-risers without blending, although lower than the ~ 60 per cent derived by Duivenvoorden et al. (2018) from mock observations using the Béthermin et al. (2017) models (note that their sources are brighter with a flux density cut of $S_{500\,\mu m} > 63$ mJy).

Fig. 16 shows the distribution of flux density ratios between the brightest component of the multiple system with respect to the total flux density of the system. Our analysis indicates that the brightest component contributes 50–75 per cent (with a median ≈ 55 per cent) at 1.1 mm. This is in agreement with results from previous works, using both interferometric and single-dish observations (e.g. Donevski et al. 2018; Ma et al. 2019; Greenslade et al. 2020).

To shed light on the multiplicity as a function of the original 500 μm flux density (i.e. before deblending) and to compare to model predictions and other studies, we have divided our sample in two flux density bins: fainter and brighter than $S_{500\,\mu m} = 60$ mJy. Fig. 17 shows the multiplicity fraction as a function of our AzTEC signal-to-noise detection threshold for the whole sample (as in Fig. 9), compared to the faint and bright sub-samples. Of the twelve *H*-ATLAS sources in our sample with $60 \leq S_{500\,\mu m} \leq 80$ mJy, seven are identified as single systems, two break into multiple components, and three have no detections (assuming a SNR threshold ≥ 4). This corresponds to a multiplicity fraction of ~ 17 per cent , which is a factor of two larger than the multiplicity of the fainter sample. This is in agreement with the SMA results from Greenslade et al. (2020)

---

[9]Note that in order to differentiate between the original and the deblended *Herschel* flux densities, we use the symbols S_λ and F_λ, respectively.

The four candidates, whose members have consistent redshifts with each others within the error bars, are shown in Fig. 13. As discussed in Section 4, these sources might trace galaxy over-densities as those recently discovered within similar samples (e.g. Oteo et al. 2018). Some of them are also in agreement with being galaxy pairs in an early-stage (pre-coalescence) merger as those predicted by simulations (e.g. Hayward et al. 2011). These systems, which given their component separations ($\Delta \gtrsim 20$ arcsec) are hard to identify with small fields-of-view interferometers, are hence ideal targets to study the environmental effects on the star formation activity and to understand the star formation process during the earliest stages of galaxy mergers.

The catalogue of AzTEC/*Herschel* sources is given in Table A1, including their updated photometry, derived physical properties, and the best high-z and physically interacting galaxy candidates.

Our results emphasize the importance of accounting for multiplicity in any conclusions derived from *Herschel*/SPIRE observations, particularly those that estimate number counts or the space density of DSFGs at high redshifts.

The fast mapping speeds of a new generation of large format cameras for the 50-m LMT (Hughes et al. 2020), e.g. MUSCAT (Brien et al. 2018) and TolTEC[10] (Bryan et al. 2018), will result in thousands of DSFGs with better photometry and position accuracy for counterpart identification. The angular resolution provided by the 50 m primary mirror of the LMT will allow the identification of multiple systems separated by, at least, angular scales $\gtrsim 5$ arcsec (i.e. $\gtrsim 40$ kpc at $z = 3$), and reduce the confusion noise by an order of magnitude (~ 0.025 mJy at 1.1 mm). This would be sufficient to resolve 50 per cent of the multiple systems identified with interferometers (e.g. Ma et al. 2019) with enough sensitivity to explore the less extreme (and more abundant) population of Luminous Infrared Galaxies ($L_{IR} \gtrsim 10^{11}$ L$_\odot$). All of these measurements combined will better constrain the space density of DSFGs and their contribution to the star formation history at the earliest stages of galaxy formation in the Universe.

Figure 17. Multiplicity fraction as a function of 1.1 mm SNR detection threshold for: the whole sample (red circles), and sources fainter (triangles) and brighter (squares) than $S_{500\,\mu m} = 60$ mJy (before deblending). The multiplicity fraction of the bright sample is ~ 2 times larger than that from the fainter sample, and should be considered by models and simulations that try to explain the bright-end of the 500 μm *Herschel* population of high-z galaxies.

who found, in a sample of 17 SPIRE $S_{500\,\mu m} > 60$ mJy sources, twelve single systems, three multiples, and two non detections (i.e. a multiplicity fraction ~ 18 per cent). We note that, although the sample from Greenslade et al. (2020) includes sources with a wider range of 500 μm flux densities (up to $S_{500\,\mu m} = 160$ mJy), they only find multiple systems or non-detections (that could potentially be associated with multiple systems) in sources with $S_{500\,\mu m} \leq 82$ mJy. These results seem to disagree with models suggesting that *Herschel* sources with $S_{500\,\mu m} > 60$ mJy are most likely single galaxies, potentially magnified by gravitational-lensing effects (e.g. Béthermin et al. 2017).

The redshift distribution of all the *Herschel*-AzTEC sources (singles and multiples) shows that ~ 33 per cent of the objects lie at $z_{phot} > 4$ and ~ 85 per cent at $z_{phot} > 3$, with a median redshift of $z_{med} \approx 3.64$ (see Fig. 11). These sources show high SFRs in the range of $\approx 900-5000$ M$_\odot$ yr^{-1} (in the absence of gravitational lensing). All of this confirms the high efficiency of the colour selection criterion to select luminous high-redshift ($z > 3$) galaxies from the *Herschel* catalogues.

In Section 4, we identified the most promising high-redshift galaxies candidates, comprising 15 single sources and three members of multiple systems with $z_{phot} > 4$. Six of these sources have already been spectroscopically confirmed at $z = 4.24-6.03$, including two new spectroscopic redshifts derived in this work using the complete 50 m diameter aperture of the LMT (see Section 2.3). The rest of the objects comprise ideal targets for future spectroscopic surveys aimed at identifying the most distant DSFGs in the Universe.

Given our $z_{phot} > 4$ sample, we estimate a lower limit for the space density of $4 < z < 6$ red DSFGs of $\approx 3 \times 10^{-7}$ Mpc^{-3} which, combined with their median SFR (≈ 2500 M$_\odot$ yr^{-1} not corrected for potential gravitational lensing effects), results in a $\gtrsim 8 \times 10^{-4}$ M$_\odot$ yr^{-1} Mpc^{-3} contribution to the obscured star formation of the Universe at these early epochs (1.5–0.9 Gyr after the big bang).

Similarly, we identified those multiple systems which could potentially be physically associated (rather than line-of-sight projections).

DATA AVAILABILITY

The datasets generated and analysed during this study are available
from the corresponding author on request.

REFERENCES

Aretxaga I., Hughes D. H., Chapin E. L., Gaztañaga E., Dunlop J. S., Ivison R. J., 2003, MNRAS, 342, 759
Aretxaga I., Hughes D. H., Dunlop J. S., 2005, MNRAS, 358, 1240
Aretxaga I. et al., 2007, MNRAS, 379, 1571
Asboth V. et al., 2016, MNRAS, 462, 1989
Bakx T. J. L. C., Eales S., Amvrosiadis A., 2020a, MNRAS, 493, 4276
Bakx T. J. L. C. et al., 2020b, MNRAS, 496, 2372
Barger A. J., Cowie L. L., Sanders D. B., Fulton E., Taniguchi Y., Sato Y., Kawara K., Okuda H., 1998, Nature, 394, 248
Béthermin M. et al., 2017, A&A, 607, A89
Bothwell M. S. et al., 2010, MNRAS, 405, 219
Bourne N. et al., 2016, MNRAS, 462, 1714
Brien T. L. R. et al., 2018, in Proc. SPIE. 10708, p. 107080M
Brisbin D. et al., 2017, A&A, 608, A15
Bryan S. et al., 2018, in Proc. SPIE. 10708, p. 107080J
Casey C. M., 2020, ApJ, 900, 68
Casey C. M., Narayanan D., Cooray A., 2014, Phys. Rep., 541, 45
Chabrier G., 2003, PASP, 115, 763
Chapman S. C., Blain A. W., Smail I., Ivison R. J., 2005, ApJ, 622, 772
Cox P. et al., 2011, ApJ, 740, 63
Cybulski R. et al., 2016, MNRAS, 459, 3287
da Cunha E. et al., 2015a, ApJ, 806, 110
da Cunha E. et al., 2015b, ApJ, 806, 110
Davé R., Finlator K., Oppenheimer B. D., Fardal M., Katz N., Kereš D., Weinberg D. H., 2010, MNRAS, 404, 1355
Donevski D. et al., 2018, A&A, 614, A33
Dowell C. D. et al., 2014, ApJ, 780, 75
Dudzevičiūtė U. et al., 2020, MNRAS, 494, 3828
Duivenvoorden S. et al., 2018, MNRAS, 477, 1099
Eales S. et al., 2010, PASP, 122, 499
Engel H. et al., 2010, ApJ, 724, 233
Erickson N., Narayanan G., Goeller R., Grosslein R., 2007, in Baker A. J., Glenn J., Harris A. I., Mangum J. G., Yun M. S., eds, ASP Conf. Ser. Vol. 375, From Z-Machines to ALMA: (Sub)Millimeter Spectroscopy of Galaxies. Astron. Soc. Pac., San Francisco, p. 71
Fudamoto Y. et al., 2017, MNRAS, 472, 2028
Greenslade J., Clements D. L., Petitpas G., Asboth V., Conley A., Pérez-Fournon I., Riechers D., 2020, MNRAS, 496, 2315
Gruppioni C. et al., 2015, MNRAS, 451, 3419
Hayward C. C., 2013, MNRAS, 432, L85
Hayward C. C., Kereš D., Jonsson P., Narayanan D., Cox T. J., Hernquist L., 2011, ApJ, 743, 159
Hayward C. C., Jonsson P., Kereš D., Magnelli B., Hernquist L., Cox T. J., 2012, MNRAS, 424, 951
Hayward C. C. et al., 2018, MNRAS, 476, 2278
Hodge J. A., da Cunha E., 2020, R. Soc. Open Source, 7, 200556
Hughes D. H. et al., 1998, Nature, 394, 241
Hughes D. H. et al., 2002, MNRAS, 335, 871
Hughes D. H. et al., 2010, Proc. SPIE. 7733, p. 773312
Hughes D. H. et al., 2020, Proc. SPIE. 11445, p. 1144522
Ivison R. J. et al., 2007, MNRAS, 380, 199
Ivison R. J. et al., 2010, A&A, 518, L35
Ivison R. J. et al., 2013, ApJ, 772, 137
Ivison R. J. et al., 2016, ApJ, 832, 78
Jiménez-Andrade E. F. et al., 2020, ApJ, 890, 171
Jin S. et al., 2019, ApJ, 887, 144
Karim A. et al., 2013, MNRAS, 432, 2
Kato Y. et al., 2018, PASJ, 70, L6
Kennicutt R. C., Evans N. J., 2012, ARA&A, 50, 531
Koprowski M. P. et al., 2016, MNRAS, 458, 4321
Lacey C. G. et al., 2016, MNRAS, 462, 3854
Lagos C. d. P. et al., 2019, MNRAS, 489, 4196
Lewis A. J. R. et al., 2018, ApJ, 862, 96
Lindner R. R. et al., 2011, ApJ, 737, 83
Ma J. et al., 2019, ApJS, 244, 30
Maddox S. J., Dunne L., 2020, MNRAS, 493, 2363*
Markwardt C. B., 2009, ASP Conf. Ser. Vol. 411, Astronomical Data Analysis Software and Systems XVIII. Astron. Soc. Pac., San Francisco, p. 251
Marrone D. P. et al., 2018, Nature, 553, 51
McAlpine S. et al., 2019, MNRAS, 488, 2440
Michałowski M., Hjorth J., Watson D., 2010, A&A, 514, A67
Michałowski M. J. et al., 2012, MNRAS, 426, 1845
Michałowski M. J. et al., 2017, MNRAS, 469, 492
Miller T. B. et al., 2018, Nature, 556, 469
Narayanan D., Hayward C. C., Cox T. J., Hernquist L., Jonsson P., Younger J. D., Groves B., 2010, MNRAS, 401, 1613
Narayanan D. et al., 2015, Nature, 525, 496
Negrello M. et al., 2010, Science, 330, 800
Negrello M. et al., 2017, MNRAS, 465, 3558
Nguyen H. T. et al., 2010, A&A, 518, L5
Oliver S. J. et al., 2012, MNRAS, 424, 1614
Oteo I. et al., 2016, ApJ, 827, 34
Oteo I. et al., 2018, ApJ, 856, 72
Planck Collaboration XIII 2016, A&A, 594, A13
Pope A., Chary R.-R., 2010, ApJ, 715, L171
Pope A. et al., 2008, ApJ, 675, 1171
Reuter C. et al., 2020, ApJ, 902, 78
Riechers D. A. et al., 2013, Nature, 496, 329
Sawicki M., 2012, PASP, 124, 1208
Scott K. S. et al., 2008, MNRAS, 385, 2225
Scott K. S. et al., 2012, MNRAS, 423, 575
Silva L., Granato G. L., Bressan A., Danese L., 1998, ApJ, 509, 103
Simpson J. M. et al., 2014, ApJ, 788, 125
Simpson J. M. et al., 2020, MNRAS, 495, 3409
Smail I., Ivison R. J., Blain A. W., 1997, ApJ, 490, L5
Stach S. M. et al., 2018, ApJ, 860, 161
Strandet M. L. et al., 2017, ApJ, 842, L15
Swinbank A. M. et al., 2010, Nature, 464, 733
Tacconi L. J. et al., 2006, ApJ, 640, 228
Toft S. et al., 2014, ApJ, 782, 68
Valiante E. et al., 2016, MNRAS, 462, 3146
Vieira J. D. et al., 2010, ApJ, 719, 763
Wardlow J. L. et al., 2013, ApJ, 762, 59
Wardlow J. L. et al., 2018, MNRAS, 479, 3879
Wilson G. W. et al., 2008, MNRAS, 386, 807
Wong O. I. et al., 2017, MNRAS, 466, 574
Yun M. S. et al., 2012, MNRAS, 420, 957
Yun M. S. et al., 2015, MNRAS, 454, 3485
Zavala J. A. et al., 2015, MNRAS, 452, 1140
Zavala J. A. et al., 2018a, Nat. Astron., 2, 56
Zavala J. A. et al., 2018b, MNRAS, 475, 5585
Zavala J. A. et al., 2021, ApJ, 909, 165
Zhang Z.-Y., Romano D., Ivison R. J., Papadopoulos P. P., Matteucci F., 2018, Nature, 558, 260

APPENDIX A: CATALOGUE AND POSTAGE STAMPS

This appendix presents $80 \times 80 \, \mathrm{arcsec}^2$ postage stamps of the 93
H-ATLAS targets included in our analysis (Fig. A1), as well as the
new photometry of the AzTEC detection (with SNR ≥ 3.5) and their
derived physical parameters Table A1.
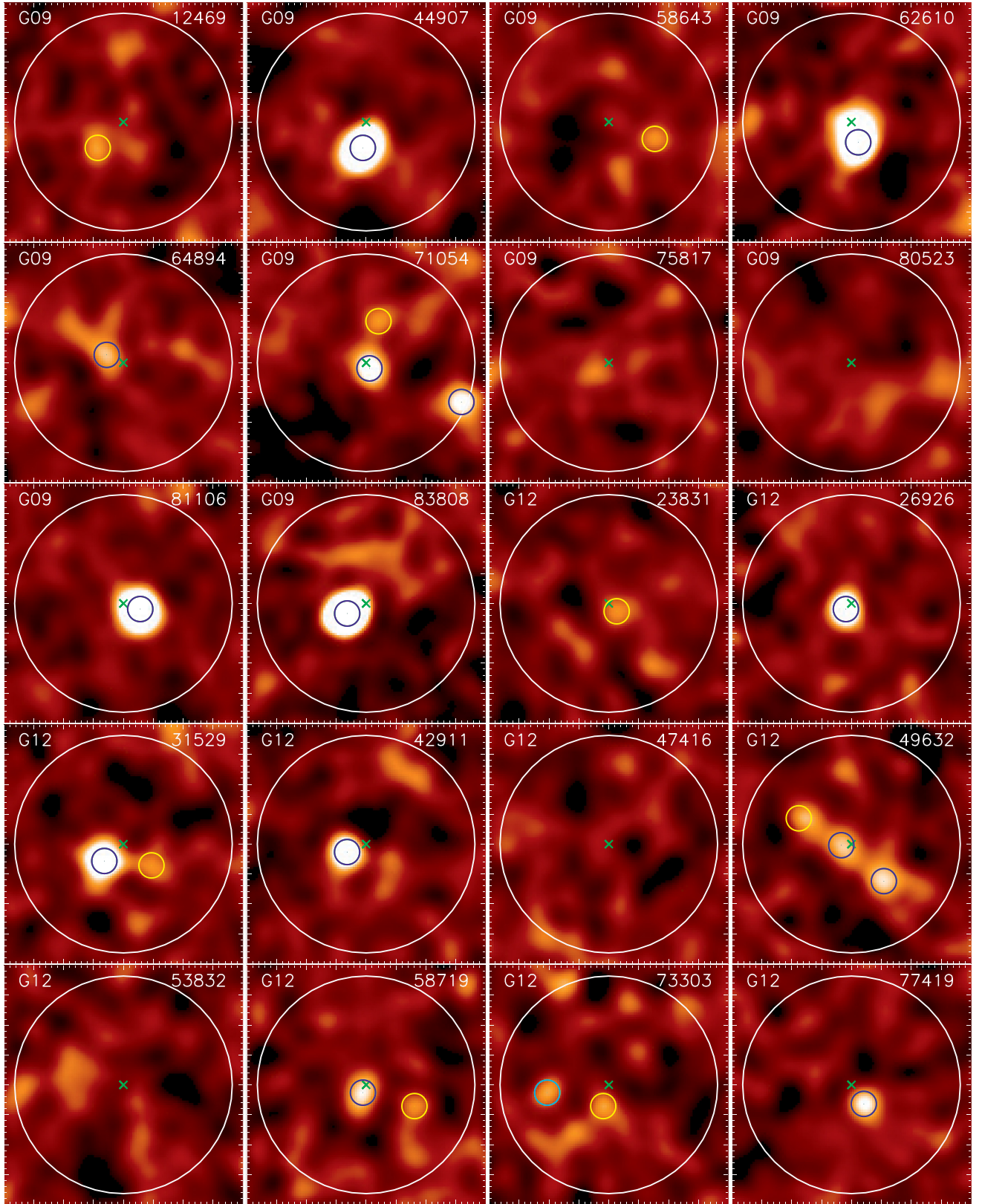
Figure A1. $80 \times 80\,\mathrm{arcsec}^2$ postage stamps of the 93 *H*-ATLAS targets included in our analysis. Images correspond to the 1.1 mm AzTEC SNR maps. Green crosses and white circles indicate the *H*-ATLAS targeted position and the adopted search radius (36.6 arcsec), respectively. Small circles (9.5 arcsec in diameter) mark the position of AzTEC detections, with: yellow corresponding to $3.0 \leq \mathrm{SNR} < 3.5$, light blue to $3.5 \leq \mathrm{SNR} < 4.0$, and dark-blue to $\mathrm{SNR} \geq 4.0$.
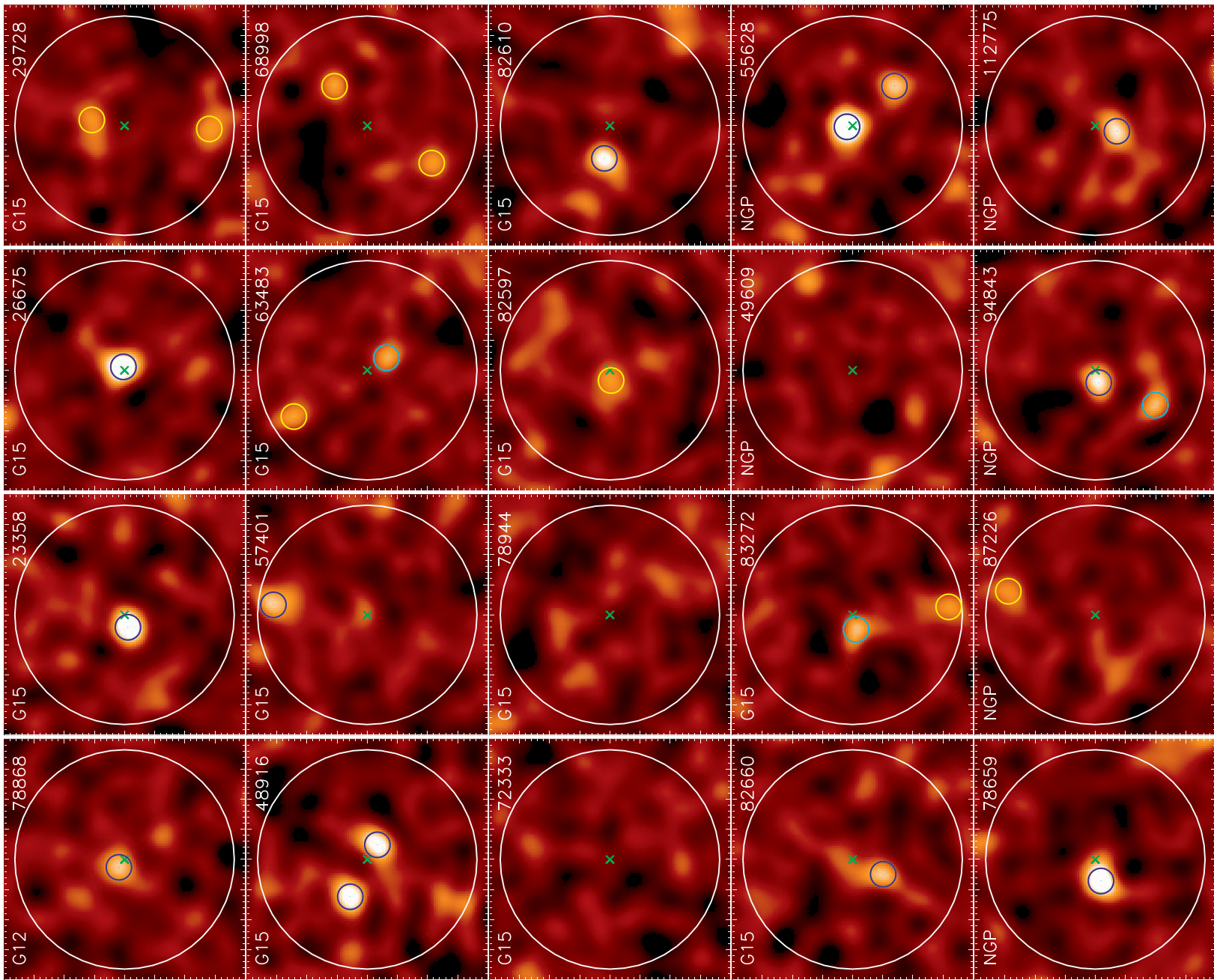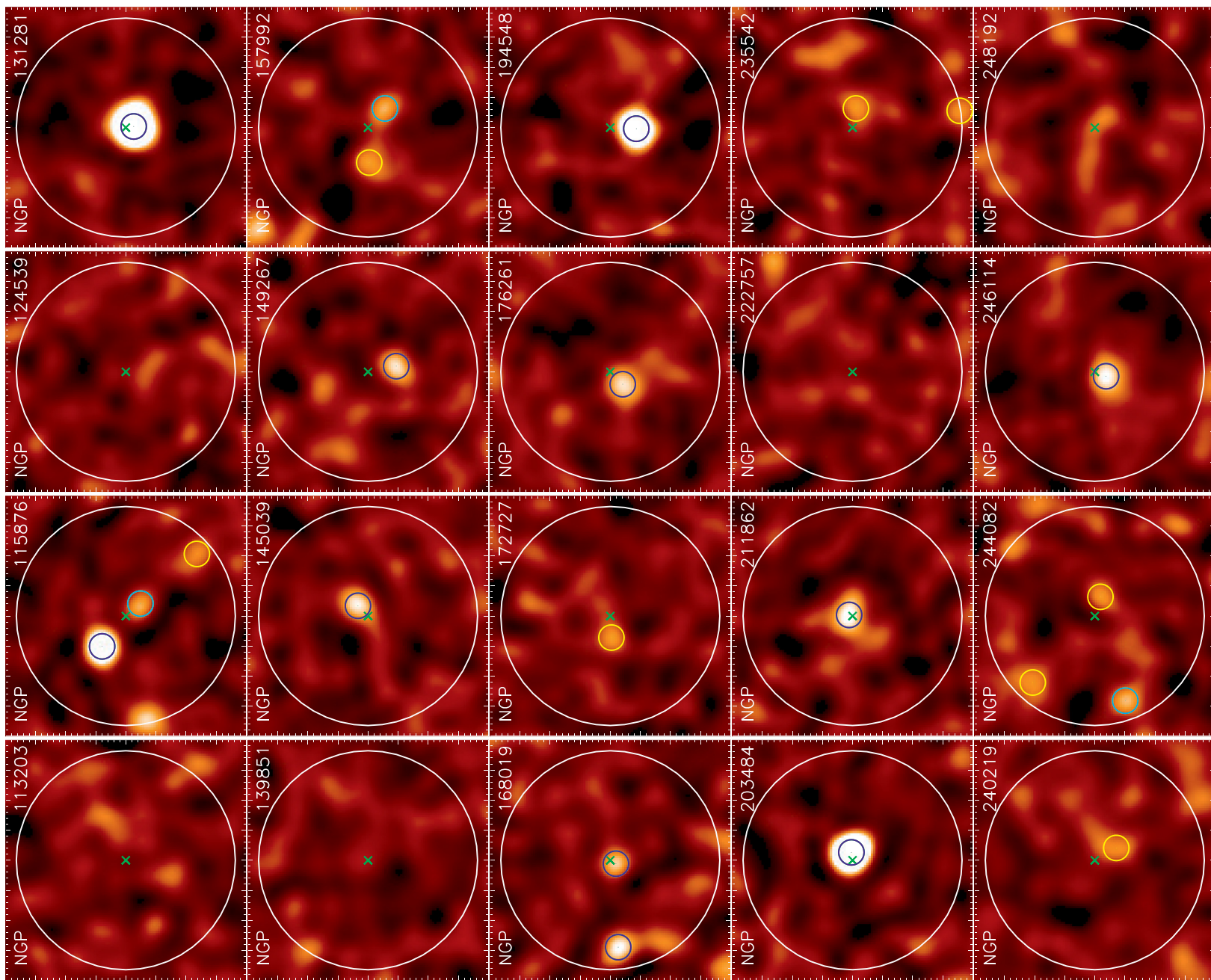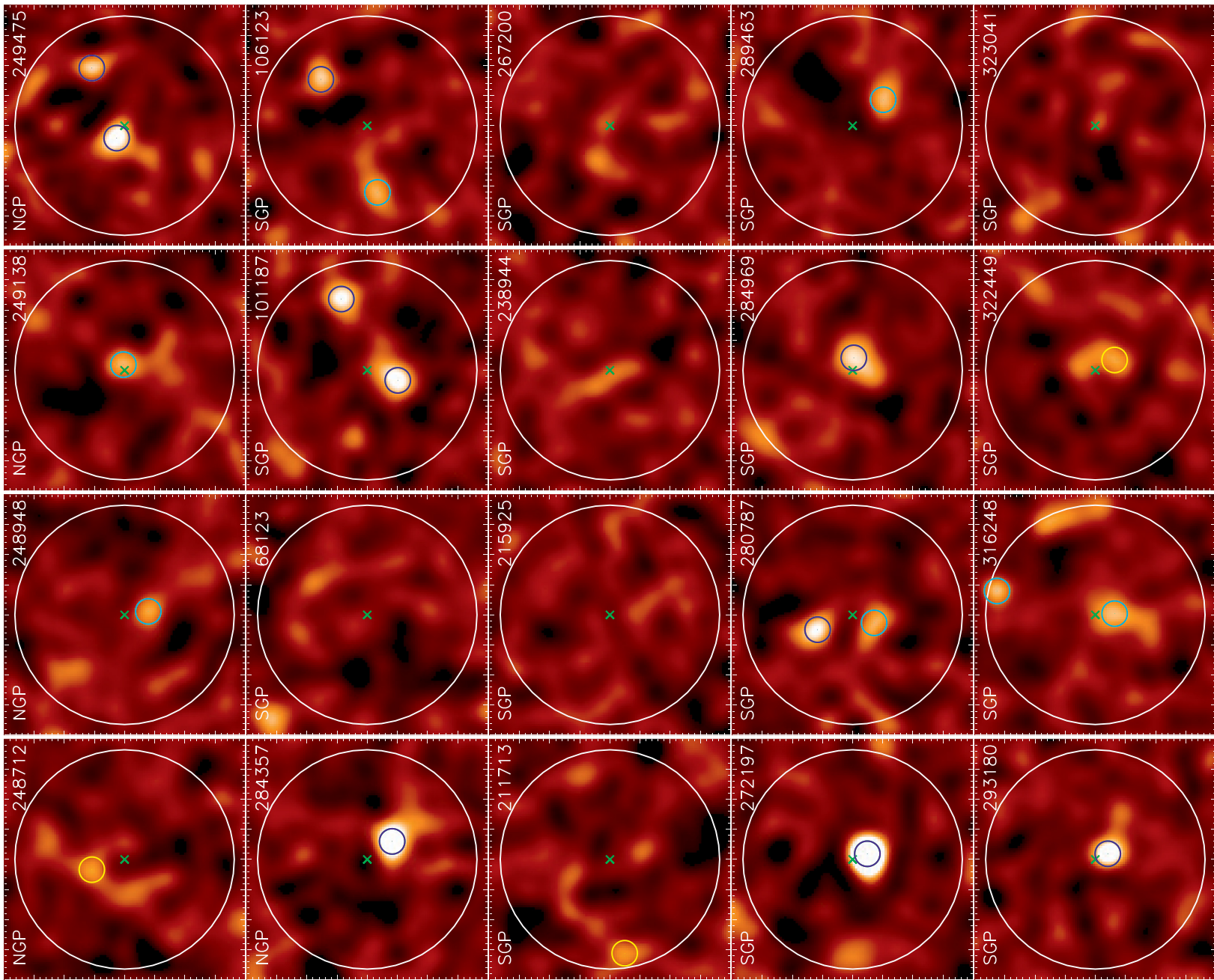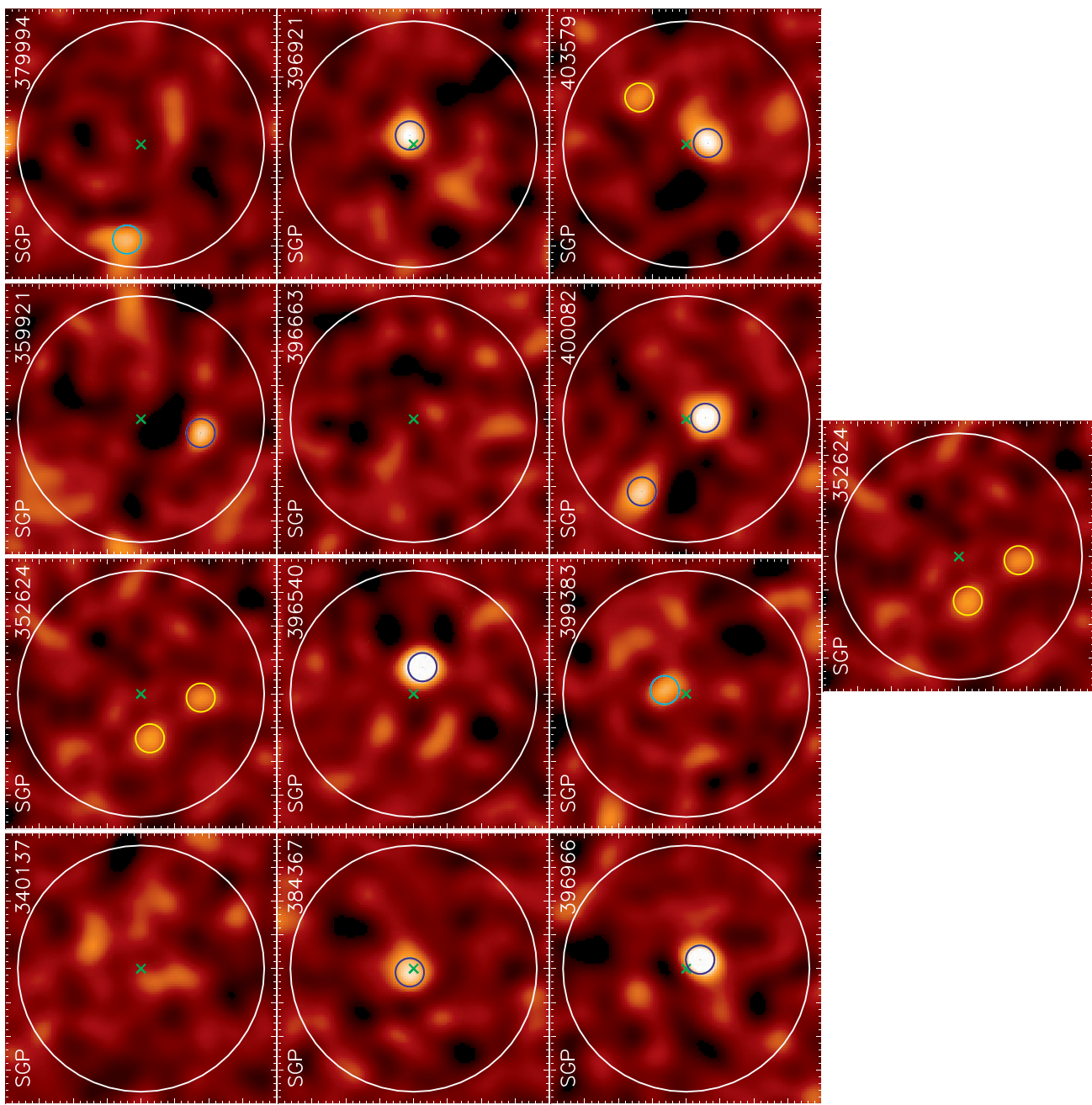
Figure A1. continued

Figure A1. continued

Figure A1. continued

Figure A1. continued

Table A1. AzTEC 1.1 mm detections with SNR ≥3.5, including deblended *Herschel*/SPIRE flux densities (columns 4–6). The AzTEC flux density and SNR are listed in columns 7 and 8. SED fitted parameters (z_{phot}, L_{IR}) and SFR are given in columns 9–11 (with dashes indicating that the fitting did not converge). The separation between the AzTEC detection and the *Herschel* position is given in column 12. The last two columns to the right indicate, for SNR detection thresholds ≥4.0 and ≥3.5, if the source is classified as single (S) or as a member of a multiple system (M). An additional P indicates that the sources are physically interacting system candidates. Our list of robust high-z (>4) candidates are indicated with their ID (first column) in boldface font.

ID	RA (deg)	Dec. (deg)	$F_{250\,\mu m}$ (mJy)	$F_{350\,\mu m}$ (mJy)	$F_{500\,\mu m}$ (mJy)	$S_{1.1\,mm}$ (mJy)	SNR_{Az}	z_{phot}	$L_{IR(8-1000\,\mu m)}$ ($10^{12}L_\odot$)	SFR ($M_\odot\,yr^{-1}$)	*Separation (arcsec)	Class 4.0σ	Class 3.5σ
G09-44907	129.345 104	1.427 174	17.1 ± 7.4	37.9 ± 7.8	49.8 ± 9.2	11.5 ± 0.9	12.5	$4.14^{+0.28}_{-0.24}$	$17.7^{+5.0}_{-4.0}$	2614^{+734}_{-586}	7.9	S	S
G09-62610	137.353 750	1.926 694	17.5 ± 6.7	36.6 ± 7.3	53.7 ± 8.4	8.1 ± 0.7	11.5	$3.58^{+0.24}_{-0.22}$	$13.5^{+3.5}_{-3.1}$	2002^{+516}_{-455}	6.7	S	S
G09-64894	138.191 354	1.195 965	19.9 ± 6.8	35.5 ± 7.5	55.4 ± 8.0	4.8 ± 1.2	4.1	$3.28^{+0.24}_{-0.24}$	$10.7^{+3.2}_{-2.8}$	1589^{+472}_{-407}	5.9	S	S
G09-71054.A	137.193 646	1.891 493	21.0 ± 7.0	39.2 ± 7.5	44.2 ± 8.9	5.4 ± 0.8	6.6	$3.16^{+0.26}_{-0.22}$	$9.9^{+3.2}_{-2.5}$	1464^{+468}_{-373}	2.2	M	M
G09-71054.B	137.185 099	1.888 368	58.9 ± 7.0	50.6 ± 7.5	30.7 ± 8.9	5.6 ± 1.0	5.6	$2.26^{+0.16}_{-0.28}$	$10.8^{+2.8}_{-3.2}$	1602^{+411}_{-475}	34.9	M	M
G09-81106^a	132.403 229	0.247 799	14.0 ± 6.0	31.0 ± 8.2	47.6 ± 8.8	11.1 ± 0.8	13.7	$4.32^{+0.32}_{-0.26}$	$16.8^{+4.9}_{-4.1}$	2482^{+721}_{-604}	6.5	S	S
G09-83808^a	135.190 729	0.689 576	9.6 ± 7.2	21.8 ± 7.4	41.6 ± 8.2	17.5 ± 0.8	21.3	$5.34^{+0.62}_{-0.34}$	$24.1^{+8.8}_{-5.5}$	3566^{+1300}_{-820}	6.2	S	S
G12-26926^a	183.489 479	−1.373 146	26.8 ± 7.0	43.1 ± 7.5	51.5 ± 8.2	14.9 ± 1.6	9.6	$4.30^{+0.22}_{-0.54}$	$25.9^{+5.6}_{-7.6}$	3839^{+825}_{-1131}	1.6	S	S
G12-31529	181.651 146	1.548 312	20.6 ± 7.4	36.8 ± 7.9	56.1 ± 9.1	8.4 ± 0.9	9.1	$3.64^{+0.22}_{-0.22}$	$14.2^{+3.7}_{-3.3}$	2096^{+551}_{-467}	7.5	S	S
G12-42911	175.812 813	0.479 035	18.2 ± 6.9	35.8 ± 7.2	48.8 ± 8.0	13.2 ± 1.5	8.9	$4.28^{+0.36}_{-0.28}$	$19.8^{+5.5}_{-4.3}$	2931^{+820}_{-637}	5.9	S	S
G12-49632.A	179.712 187	−0.167 757	<7.0	12.9 ± 7.5	<9.5	5.2 ± 1.1	4.7	−	−	−	16.4	M	M
G12-49632.B	179.716 146	−0.164 424	21.7 ± 7.0	31.7 ± 7.5	40.1 ± 9.5	4.6 ± 1.1	4.3	$3.14^{+0.34}_{-0.32}$	$8.7^{+3.4}_{-2.4}$	1293^{+500}_{-419}	2.7	M	M
G12-58719	185.308 854	0.930 396	28.2 ± 7.8	45.1 ± 8.1	58.1 ± 8.9	6.7 ± 1.3	5.0	$3.26^{+0.26}_{-0.32}$	$13.3^{+3.9}_{-3.7}$	1971^{+578}_{-544}	1.9	S	S
G12-73303	183.514 691	−1.933 354	<6.9	19.9 ± 7.6	34.8 ± 8.6	4.1 ± 1.2	3.5	$3.62^{+0.46}_{-0.62}$	$7.7^{+4.2}_{-3.7}$	1137^{+614}_{-544}	10.0	-	S
G12-77419	182.269 896	−1.090 979	13.3 ± 7.9	31.2 ± 8.0	48.1 ± 9.1	8.7 ± 1.6	5.3	$4.00^{+0.36}_{-0.32}$	$14.6^{+5.1}_{-4.2}$	2156^{+755}_{-628}	7.5	S	S
G12-78868	179.059 688	1.652 340	11.9 ± 7.6	34.0 ± 7.9	43.6 ± 8.5	10.1 ± 2.4	4.2	$4.18^{+0.42}_{-0.40}$	$16.4^{+6.1}_{-5.0}$	2432^{+899}_{-732}	3.2	S	S
G15-23358	214.860 938	0.193 757	29.3 ± 6.9	51.3 ± 7.4	59.7 ± 8.3	7.1 ± 1.0	6.9	$2.94^{+0.36}_{-0.14}$	$11.9^{+2.5}_{-0.9}$	1758^{+366}_{-137}	3.4	S	S
G15-26675	221.138 229	0.278 007	23.1 ± 6.9	54.6 ± 7.3	61.9 ± 7.8	11.7 ± 1.8	6.7	$3.52^{+0.38}_{-0.14}$	$15.9^{+2.8}_{-1.0}$	2356^{+416}_{-149}	2.2	S	S
G15-48916.A	214.619 063	0.790 826	15.8 ± 7.0	27.7 ± 7.3	22.7 ± 8.3	6.2 ± 1.1	5.8	$3.84^{+0.48}_{-0.58}$	$9.6^{+4.7}_{-4.0}$	1420^{+700}_{-592}	13.3	MP	MP
G15-48916.B	214.614 271	0.788 326	18.1 ± 7.0	23.4 ± 7.3	23.4 ± 8.3	6.0 ± 1.0	5.8	$3.50^{+0.64}_{-0.34}$	$10.2^{+6.4}_{-3.5}$	1508^{+941}_{-521}	6.2	MP	MP
G15-57401	214.028 437	1.168 215	31.6 ± 6.8	43.3 ± 7.6	39.7 ± 8.3	4.7 ± 1.1	4.3	$2.84^{+0.26}_{-0.26}$	$9.4^{+3.1}_{-2.5}$	1387^{+460}_{-375}	32.1	S	S
G15-63483	221.294 479	0.016 271	19.9 ± 6.8	32.9 ± 7.5	41.1 ± 8.3	5.1 ± 1.4	3.6	$2.92^{+0.44}_{-0.32}$	$10.4^{+5.0}_{-3.4}$	1537^{+743}_{-498}	7.4	-	S
G15-82610	220.731 980	1.163 035	13.0 ± 6.8	30.1 ± 7.6	43.2 ± 9.0	7.2 ± 1.3	5.3	$3.86^{+0.36}_{-0.32}$	$12.2^{+4.5}_{-3.6}$	1801^{+668}_{-534}	10.5	S	S
G15-82660	215.636 146	0.503 090	22.6 ± 7.5	52.1 ± 8.1	75.9 ± 9.0	4.3 ± 1.0	4.2	$2.68^{+0.42}_{-0.12}$	$10.2^{+2.8}_{-0.8}$	1507^{+411}_{-112}	10.2	S	S
G15-83272	213.803 646	−0.276 910	16.3 ± 7.5	31.6 ± 7.8	54.9 ± 8.8	6.7 ± 1.7	4.0	$3.78^{+0.32}_{-0.30}$	$13.2^{+4.5}_{-3.8}$	1952^{+671}_{-561}	4.1	-	S
NGP-112775	204.170 765	26.264 535	25.2 ± 7.2	33.3 ± 7.5	39.6 ± 8.4	6.2 ± 1.3	4.8	$3.32^{+0.32}_{-0.36}$	$10.8^{+3.7}_{-3.4}$	1603^{+551}_{-500}	6.5	S	S
NGP-115876.A	204.653 354	27.548 868	16.6 ± 7.7	22.2 ± 8.6	15.2 ± 10.9	13.8 ± 1.4	10.0	$5.02^{+1.00}_{-0.62}$	$21.0^{+14.3}_{-8.9}$	3104^{+2113}_{-1323}	13.7	S	M
NGP-115876.B	204.648 889	27.545 326	28.1 ± 7.7	43.8 ± 8.5	50.1 ± 10.4	5.0 ± 1.4	3.6	$2.48^{+0.28}_{-0.30}$	$10.4^{+4.1}_{-3.4}$	1543^{+610}_{-499}	6.9	-	M
NGP-131281	193.200 871	34.403 757	26.6 ± 7.6	55.3 ± 8.4	72.7 ± 9.5	19.1 ± 1.3	15.0	$4.22^{+0.20}_{-0.18}$	$28.8^{+5.4}_{-4.6}$	4264^{+798}_{-676}	2.3	S	S
NGP-145039	194.371 603	29.281 424	32.5 ± 7.6	42.9 ± 7.9	51.4 ± 8.7	6.0 ± 1.2	4.9	$3.08^{+0.22}_{-0.24}$	$11.7^{+3.2}_{-2.9}$	1736^{+477}_{-442}	6.3	S	S
NGP-149267	203.000 852	26.419 826	23.2 ± 7.6	46.7 ± 7.9	52.1 ± 8.4	6.2 ± 1.3	4.7	$3.26^{+0.22}_{-0.22}$	$12.4^{+3.3}_{-2.9}$	1838^{+486}_{-435}	9.1	S	S
NGP-157992	193.515 275	27.176 396	22.9 ± 7.6	46.2 ± 8.1	57.8 ± 8.6	9.3 ± 2.5	3.7	$3.74^{+0.22}_{-0.44}$	$17.9^{+4.4}_{-5.3}$	2642^{+655}_{-784}	9.4	-	S
NGP-168019.B	205.414 677	32.476 257	60.3 ± 7.5	85.7 ± 8.3	82.5 ± 9.3	8.2 ± 1.6	5.2	$2.58^{+0.22}_{-0.14}$	$14.3^{+2.1}_{-1.3}$	2120^{+312}_{-192}	33.4	M	M
NGP-168019.A	205.405 540	32.476 465	28.0 ± 7.5	50.1 ± 8.2	51.2 ± 9.5	6.5 ± 1.5	4.3	$3.20^{+0.26}_{-0.26}$	$12.9^{+3.8}_{-3.3}$	1912^{+567}_{-486}	1.2	M	M
NGP-176261	199.243 213	33.915 007	24.3 ± 7.5	40.0 ± 7.9	52.7 ± 8.7	7.3 ± 1.6	4.7	$3.48^{+0.38}_{-0.26}$	$13.7^{+3.8}_{-3.4}$	2032^{+567}_{-506}	5.3	S	S
NGP-194548^a	203.406 969	24.259 451	17.9 ± 7.6	47.1 ± 8.0	67.9 ± 8.7	13.8 ± 1.3	11.1	$3.80^{+0.42}_{-0.14}$	$18.0^{+3.2}_{-1.0}$	2661^{+474}_{-154}	7.9	S	S

ID	RA (deg)	Dec. (deg)	$F_{250\,\mu m}$ (mJy)	$F_{350\,\mu m}$ (mJy)	$F_{500\,\mu m}$ (mJy)	$S_{1.1\,mm}$ (mJy)	SNR_{Az}	z_{phot}	$L_{IR(8-1000\,\mu m)}$ $(10^{12} L_\odot)$	SFR $(M_\odot\,yr^{-1})$	*Separation (arcsec)	Class 4.0σ	Class 3.5σ
NGP-203484[a]	204.915 985	31.369 396	20.9 ± 7.7	38.5 ± 7.9	51.1 ± 9.0	21.3 ± 1.4	15.4	$5.18^{+0.26}_{-0.54}$	$35.0^{+6.9}_{-8.6}$	5173^{+1023}_{-1268}	4.1	S	S
NGP-211862	193.669 650	26.824 187	28.2 ± 7.5	45.7 ± 8.1	45.1 ± 9.1	8.1 ± 1.5	5.4	$3.38^{+0.26}_{-0.26}$	$13.9^{+4.0}_{-3.5}$	2054^{+595}_{-512}	2.3	S	S
NGP-244082	199.496 726	34.488 118	<7.6	16.2 ± 8.2	35.7 ± 9.0	6.6 ± 1.7	3.9	$4.36^{+0.72}_{-0.84}$	$10.6^{+7.3}_{-5.6}$	1574^{+1074}_{-824}	34.5	-	S
NGP-246114[a]	205.308 501	33.993 556	17.3 ± 6.5	30.4 ± 8.1	33.9 ± 8.5	7.8 ± 1.5	5.2	$3.80^{+0.48}_{-0.34}$	$12.3^{+5.1}_{-3.7}$	1820^{+754}_{-544}	3.1	S	S
NGP-248948	192.159 401	29.626 687	9.1 ± 7.8	31.3 ± 8.2	44.5 ± 8.8	9.6 ± 2.7	3.5	$3.64^{+0.64}_{-0.50}$	$16.6^{+8.5}_{-5.9}$	2451^{+1254}_{-875}	7.5	-	S
NGP-249138	193.610 448	24.625 757	21.3 ± 7.6	40.5 ± 8.0	57.7 ± 8.9	7.2 ± 1.9	3.8	$3.60^{+0.26}_{-0.26}$	$14.8^{+4.2}_{-3.7}$	2195^{+625}_{-542}	3.1	-	S
NGP-249475.A	206.236 099	31.442 021	14.8 ± 7.5	33.6 ± 8.2	40.6 ± 9.8	8.4 ± 1.4	5.8	$3.94^{+0.40}_{-0.34}$	$13.5^{+5.4}_{-4.2}$	1994^{+792}_{-615}	5.2	M	M
NGP-249475.B	206.228 529	31.444 312	13.9 ± 7.5	12.6 ± 8.2	<9.8	6.5 ± 1.5	4.5	$4.62^{+2.12}_{-0.66}$	$9.9^{+19.0}_{-6.9}$	1471^{+2817}_{-1020}	26.0	M	M
NGP-284357[a]	203.215 088	33.394 556	12.6 ± 5.3	20.4 ± 7.8	42.4 ± 8.3	11.1 ± 1.4	7.7	$4.70^{+0.44}_{-0.36}$	$16.5^{+5.8}_{-4.5}$	2442^{+859}_{-671}	11.0	S	S
NGP-55628.A	206.604 457	34.271 562	42.0 ± 8.0	47.9 ± 8.4	60.5 ± 10.8	10.8 ± 1.4	7.6	$3.52^{+0.16}_{-0.40}$	$20.6^{+4.3}_{-5.8}$	3055^{+630}_{-853}	2.7	M	M
NGP-55628.B	206.599 920	34.267 187	46.0 ± 8.0	59.0 ± 8.4	35.5 ± 10.7	6.1 ± 1.5	4.2	$2.66^{+0.20}_{-0.36}$	$11.1^{+3.2}_{-3.6}$	1645^{+466}_{-527}	21.3	M	M
NGP-78659	207.218 236	26.898 910	30.8 ± 7.5	53.3 ± 7.9	67.8 ± 8.4	14.6 ± 2.2	6.8	$3.90^{+0.24}_{-0.22}$	$23.7^{+5.1}_{-4.4}$	3506^{+755}_{-649}	7.2	S	S
NGP-94843.A	204.696 040	25.669 062	33.6 ± 7.7	42.3 ± 8.2	54.8 ± 10.6	6.7 ± 1.4	5.0	$3.16^{+0.24}_{-0.26}$	$12.5^{+3.7}_{-3.2}$	1842^{+551}_{-475}	3.7	S	MP
NGP-94843.B	204.698 351	25.663 854	27.5 ± 7.7	31.8 ± 8.2	28.5 ± 10.6	5.5 ± 1.4	3.9	$3.22^{+0.30}_{-0.56}$	$10.5^{+4.4}_{-651}$	1554^{+646}_{-651}	22.6	-	MP
SGP-101187.A	16.970 845	−30.299 799	<7.9	35.1 ± 8.1	48.6 ± 9.3	6.0 ± 1.1	5.7	$3.48^{+0.30}_{-0.28}$	$10.9^{+4.0}_{-3.2}$	1611^{+593}_{-470}	9.7	M	M
SGP-101187.B	16.962 158	−30.294 590	42.7 ± 7.9	68.3 ± 8.1	71.2 ± 9.3	6.1 ± 1.1	5.3	$2.84^{+0.14}_{-0.20}$	$14.0^{+2.8}_{-449}$	2073^{+415}_{-449}	29.8	M	M
SGP-106123.A	13.846 177	−28.005 632	<7.9	63.5 ± 8.6	59.3 ± 9.6	4.3 ± 1.0	4.3	$2.94^{+0.22}_{-0.36}$	$10.5^{+3.2}_{-496}$	1552^{+479}_{-496}	24.4	S	MP
SGP-106123.B	13.857 975	−28.010 840	<7.9	29.8 ± 8.6	38.3 ± 9.6	3.5 ± 1.0	3.7	$2.90^{+0.52}_{-0.30}$	$5.8^{+1.8}_{-1.0}$	860^{+265}_{-143}	24.4	-	MP
SGP-272197[a]	1.530 803	−32.445 340	<7.4	18.6 ± 8.2	46.1 ± 8.6	21.1 ± 1.5	13.8	$5.76^{+0.74}_{-0.40}$	$28.6^{+11.3}_{-7.3}$	4229^{+1672}_{-1073}	5.2	S	S
SGP-280787.A	350.395 117	−33.077 812	<7.5	11.6 ± 8.1	<13.8	9.6 ± 1.8	5.2	−	−	−	13.3	S	M
SGP-280787.B	350.394 372	−33.083 021	<7.5	24.2 ± 8.1	55.4 ± 8.6	7.0 ± 1.9	3.7	$4.00^{+0.36}_{-0.34}$	$13.8^{+5.0}_{-4.1}$	2042^{+738}_{-606}	6.8	-	M
SGP-284969	15.856 769	−30.058 979	<7.8	29.5 ± 8.2	44.2 ± 9.5	4.0 ± 0.8	4.7	$3.04^{+0.44}_{-0.26}$	$6.3^{+1.5}_{-0.9}$	929^{+222}_{-128}	5.7	S	S
SGP-289463	25.533 576	−32.576 882	<7.8	27.8 ± 8.5	59.0 ± 9.5	7.7 ± 2.0	3.9	$4.00^{+0.34}_{-0.34}$	$14.9^{+5.2}_{-4.5}$	2202^{+766}_{-667}	14.6	-	S
SGP-293180	18.159 985	−30.784 299	14.4 ± 7.8	23.9 ± 7.8	38.5 ± 8.7	7.3 ± 1.1	6.5	$4.02^{+0.42}_{-0.42}$	$11.7^{+4.9}_{-4.1}$	1734^{+720}_{-607}	4.6	S	S
SGP-316248.B	354.390 415	−34.829 924	<11.2	<11.8	<14.4	5.8 ± 1.5	4.0	−	−	−	35.0	-	M
SGP-316248.A	354.392 953	−34.840 757	20.4 ± 7.2	24.2 ± 7.6	48.5 ± 8.9	5.3 ± 1.3	4.0	$3.48^{+0.34}_{-0.34}$	$10.1^{+3.9}_{-3.2}$	1501^{+569}_{-472}	5.8	-	M
SGP-359921	16.920 650	−28.453 187	13.0 ± 8.0	24.2 ± 8.5	41.2 ± 9.3	4.9 ± 1.1	4.3	$3.32^{+0.60}_{-0.28}$	$7.3^{+2.2}_{-1.0}$	1072^{+325}_{-143}	17.3	S	S
SGP-379994	11.365 272	−32.553 340	<7.5	18.0 ± 8.2	29.9 ± 9.3	4.4 ± 1.1	3.9	$4.00^{+1.14}_{-0.78}$	$7.3^{+8.0}_{-4.3}$	1078^{+1179}_{-640}	32.9	-	S
SGP-384367	21.078 458	−32.979 812	<7.6	27.0 ± 8.1	51.0 ± 9.1	4.8 ± 1.0	4.6	$3.32^{+0.44}_{-0.24}$	$7.3^{+1.6}_{-0.8}$	1072^{+236}_{-123}	1.9	S	S
SGP-396540	10.268 114	−28.222 993	9.8 ± 7.5	12.8 ± 8.0	42.5 ± 8.8	9.6 ± 1.3	7.5	$4.66^{+0.54}_{-0.54}$	$14.3^{+6.8}_{-5.4}$	2120^{+999}_{-799}	10.0	S	S
SGP-396921	16.554 353	−28.230 701	<7.6	23.2 ± 8.1	49.6 ± 9.2	4.5 ± 0.9	5.2	$3.22^{+0.50}_{-0.24}$	$6.9^{+1.8}_{-0.8}$	1021^{+266}_{-122}	4.3	S	S
SGP-396966	8.877 234	−31.505 854	20.4 ± 7.8	30.5 ± 7.8	53.4 ± 8.9	8.6 ± 1.2	6.9	$3.76^{+0.28}_{-0.26}$	$13.9^{+4.2}_{-3.4}$	2060^{+619}_{-501}	5.2	S	S
SGP-399383	20.202 309	−30.974 549	24.9 ± 7.7	21.3 ± 8.3	44.4 ± 8.9	4.6 ± 1.3	3.7	$3.24^{+0.36}_{-0.44}$	$8.9^{+3.9}_{-3.4}$	1312^{+572}_{-499}	7.5	-	S
SGP-400082.A	8.385 889	−30.081 937	<7.8	20.6 ± 8.5	34.2 ± 10.2	7.5 ± 1.3	5.8	$4.56^{+0.88}_{-0.6.0}$	$11.2^{+8.4}_{-6.0}$	1658^{+1239}_{-893}	5.0	MP	MP
SGP-400082.B	8.392 871	−30.076 729	18.1 ± 7.8	14.3 ± 8.5	29.8 ± 10.2	6.6 ± 1.5	4.4	$4.56^{+1.16}_{-0.92}$	$10.1^{+9.7}_{-5.9}$	1489^{+1433}_{-876}	27.6	MP	MP
SGP-403579	355.064 638	−30.446 674	<7.6	<8.0	32.2 ± 8.5	6.1 ± 1.2	5.2	$4.30^{+0.76}_{-0.84}$	$9.5^{+6.9}_{-5.1}$	1412^{+1023}_{-756}	5.8	S	S

[a] Redshifts >4 have been spectroscopically confirmed (see Table 2 and Section 4.1).

^{1}*Consejo Nacional de Ciencia y Tecnología, Av. Insurgentes Sur 1582, Col. Crédito Constructor, Alcaldía Benito Juárez, C.P. 03940, Ciudad de México, México*

^{2}*Instituto Nacional de Astrofísica Óptica y Electrónica, Luis Enrique Erro 1, Tonantzintla CP 72840, Puebla, México*

^{3}*Department of Astronomy, The University of Texas at Austin, 2515 Speedway Blvd Stop C1400, Austin, TX 78712, USA*

^{4}*European Southern Observatory, Karl-Schwarzschild-Straße 2, D-85748 Garching, Germany*

^{5}*Department of Astronomy, University of Massachusetts, Amherst, MA 01003, USA*

^{6}*Astronomical Observatory Institute, Faculty of Physics, Adam Mickiewicz University, ul. Słoneczna 36, 60-286 Poznań, Poland*

^{7}*1QB Information Technologies (1QBit), 1285 W Pender St Unit 200, Vancouver, BC V6E 4B1, Canada*

^{8}*Institut de Radioastronomie Millimétrique, Domaine Universitaire, 300 rue de la Piscine, F-38406 Saint-Martin-d'Hères, France*

^{9}*Instituto de Radioastronomía y Astrofísica, UNAM, Campus Morelia, Morelia C.P. 58089, México*

^{10}*Instituto de Astrofísica de Canarias (IAC), E-38205 La Laguna, Tenerife, Spain*

^{11}*Universidad de La Laguna, Dpto. Astrofísica, E-38206 La Laguna, Tenerife, Spain*

^{12}*Institute for Astronomy, University of Edinburgh, Royal Observatory, Edinburgh, EH9 3HJ, UK*

^{13}*School of Physics and Astronomy, Cardiff University, Queens Buildings, The Parade, Cardiff, CF24 3AA, UK*

^{14}*Escuela Nacional de Estudios Superiores Unidad Morelia, Universidad Nacional Autónoma de México, Morelia, 58190, México*

^{15}*Institut d'Astrophysique de Paris, 98bis Bd Arago, F-75014, Paris, France*

^{16}*School of Physical Sciences, The Open University, Milton Keynes, MK7 6AA, UK*

^{17}*Department of Physics and Astronomy, University of Hawai'i at Manoa, Honolulu, Hawai'i 96822, USA*

^{18}*Leiden Observatory, Leiden University, PO Box 9513, NL-2300 RA Leiden, the Netherlands*

^{19}*Universidad de las Américas Puebla. Ex Hacienda Sta. Catarina Mártir S/N. San Andrés Cholula, Puebla 72810, México*

This paper has been typeset from a TEX/LATEX file prepared by the author.